Tests of a Silicon Strip Detector with the QWEAK Amplifier Discriminator Board (QWAD)

by

Ryan Matthew Spies

A thesis submitted to
The Faculty of Graduate Studies of
The University of Manitoba
in partial fulfillment of the requirements
of the degree of

Master of Science

Department of Physics and Astronomy
The University of Manitoba
Winnipeg, Manitoba, Canada
January 2018

Thesis advisor

Dr. Juliette Mammei

Author

Ryan Matthew Spies

Tests of a Silicon Strip Detector with the QWEAK Amplifier Discriminator Board (QWAD)

Abstract

The Hall A Compton Polarimeter at Thomas Jefferson National Accelerator Facility (JLab) utilizes a multi-plane silicon strip detector for determining the overall polarization of an electron beam. Techniques such as Compton polarimetry are an essential part of several particle physics experiments, including the Lead Radius Experiment (PREX) and the Calcium Radius Experiment (CREX). The QWEAK Amplifier Discriminator (QWAD) board is used in conjunction with a single plane of the silicon strip detector. All the properties of the board were explored, and a series of experiments were devised to determine the extent of its functionality with the silicon strip detector. Digital rate tests were performed in order to establish the functionality of the QWAD in this application.

Acknowledgments

Foremost, I would like to thank my advisor, Dr. Juliette Mammei, for taking me on as her student during this time. From start to finish I have learned so much under her guidance. It has been a privilege to work on this project with her, and I wish her and the rest of her research team success in the future.

Secondly, I am grateful to the other members of my thesis defence committee, Dr. Gerald Gwinner and Dr. Jennifer van Wijngaarden, for their quick turnaround on my thesis edits and for taking their time to take part in the examination process.

My thanks go out to the members of the Hall A Compton Polarimetry team at Jefferson Lab, especially like to thank Dave Gaskell, Alexandre Camsonne, and Josh Hoskins for their invaluable help in understanding and setting up the QWAD.

Further thanks goes out to my fellow graduate students, Sakib Rahman, Iris Halilovic, and Han Soul Lee for their help in setting up the lab with me.

I would also like to thank the professors and staff here in the Physics and Astronomy department for both their guidance and support in my coursework, especially Dr. Jie Pan for her help in setting up the QWAD experimental setup, and Dr. Peiqing Wang for providing equipment to resolve many technological issues. Thanks is also extended to Maiko Langelaar, Dr Ruth Cameron, Andiry Yamchuk, Susan Beshta, and Dr. Robert Stamps for their help and support.

I am very thankful for the community at First Unitarian Universalist, and also my Aikido dojo here at the University of Manitoba, for giving me a sense of grounding and serenity during my time here in Winnipeg.

Merci beaucoup à ma chéri, Zoée, pour ton support pendant les derniers mois pour la finition de ma thèse.

To my family back in the States and over in Ireland, I would also like to thank y'all for your help in my time here at graduate school while I've been away in Canada. I would especially like to thank my sister, Anna Murphy, for her help in brainstorming data analysis techniques.

Finally, I would also like to thank all the local friends who I have made during these years. Gabriel, Brendan, Theo, Bryce, Julia, Jason, Diana, Bryanne, Tom, and all others too numerous to list.

Thanks y'all. Merci beaucoup tout le monde. Y'all have helped me during my time in Winnipeg, and I will never forget the sense of community I felt during my time at the University of Manitoba for as long as I live.

To my Grandfather, Lealon Wimpee, who I will always remember as a man of the slide rule, and who got me interested in nuclear science.

Contents

Abstract ii
Acknowledgments iv
Dedication vi
Table of Contents ix
List of Figures x
List of Tables xi

1 Introduction **1**

2 Theory and Motivation **5**
2.1 Spin-Dependent Parity Violation 5
2.1.1 Parity-Violating Electron Scattering 6
2.1.2 The Weak Interaction 7
2.2 Compton Interaction 8
2.2.1 Kinematics 8
2.2.2 Cross-Section and Asymmetry of Polarized Compton Interaction 12
2.2.3 Compton Polarimeter 15
2.3 Electron Detector Operation 16
2.3.1 Measuring Scattered Electron Momentum 17
2.3.2 Semiconductor Detector Principles of Operation 20
2.3.3 QWAD 21

3 Methodology **28**
3.1 Rate, Threshold 28
3.1.1 Rate Tests 29
3.1.2 Threshold Tests 32
3.1.3 QWAD Modifications 35
3.2 The Experimental Setup 37
3.2.1 Test Bench Design 38
3.2.2 Timing 43
3.2.3 Noise 46

4 Results and Analysis **48**
4.1 Analysis of Rate Tests 48
4.1.1 Counting 48
4.1.2 Rates and Uncertainties 49
4.2 Results of Rate Tests 52
4.2.1 Rates 52
4.2.2 Relative Efficiencies 52

5 Conclusion **56**

A QWAD Details **59**
A.1 Test Pulse Responses 59
A.2 Silicon Detector Response 60
A.3 DAQ Timing 61

B Full Results for Digital Rates Tests **64**

Bibliography **69**

List of Figures

2.1 The weak interaction between a nucleus and an electron 8
2.2 Compton interaction and reaction planes 9
2.3 Example simulated Compton cross-section and asymmetry for a 3.3GeV beam 12
2.4 Compton Chicane diagram 16
2.5 Displacement of electrons in the Compton Polarimeter 24
2.6 Semiconductor Detector Operation 25
2.7 QWAD Board 26
2.8 QWAD Circuit Diagram 27

3.1 V1495 rate test 29
3.2 Logic Diagram of V1495 31
3.3 QWAD Pulse Response 33
3.4 Solution employed to modify the threshold of the QWAD 35
3.5 Scintillator paddle setup 39
3.6 VME crate 44
3.7 QWAD Repsonse to Silicon Detector Event 45
3.8 Periodic noise 47

4.1 Relative efficiencies for the runs with a source 55

A.1 LVDS demonstration 60
A.2 Analog QWAD Response 61
A.3 Beta response 62
A.4 Timing 63

List of Tables

3.1 Threshold Voltages for Centre QWAD Channel Bank 38

4.1 Collected rates for all runs 53
4.2 Relative efficiencies for selected runs 54

B.1 Total hits in channels for source tests. 65
B.2 Total hits in channels for background tests. 66
B.3 Single hits in channels for source tests. 67
B.4 Single hits in channels for background tests. 68

Chapter 1

Introduction

There are four main interactions in the current Standard Model of particle physics: gravitation, electromagnetism, the strong force, and the weak force. Of these four forces, the weak force is the only force which violates parity. Parity is a quantum mechanical operation that inverts spatial coordinates, and if an interaction is invariant under parity then parity is conserved. Understanding parity-violating scattering processes is therefore of interest to nuclear physicists in furthering our understanding of the weak force.

The Pb Radius Experiment (PREX) and the Ca Radius Experiment (CREX) at Jefferson Lab (JLab) are two examples of experiments that use a parity-violating scattering process, the weak scattering of electrons with the nucleus, to understand the neutron radius of the nuclei of ^{208}Pb and ^{48}Ca respectively. A longitudinally polarized beam of electrons scatters from a lead or calcium target of the respective isotope, and both slow and rapid helicity reversals are used to alternate between polarization states. It is through the measurement of scattering asymmetries A between scattering

processes which depend on the two possible helicity states of the electron beam at JLab, which are of the form:

$$A = \frac{\sigma^+ - \sigma^-}{\sigma^+ + \sigma^-}, \tag{1.1}$$

where σ is a scattering cross-section for the positive (+) or negative (-) helicity state, that the portion of scatters due to the weak interaction are isolated. This scattering asymmetry is found by applying multiple corrections to an experimentally measured asymmetry, of which the polarization of the electron beam is an essential correction. This quantity requires the measurement of the polarization.

Having a method for measuring the polarization of a beam of particles, or polarimetry, is important for making corrections on measurements where knowing the helicity state of the beam is necessary. Ideally, the beam would be 100% in the same helicity state. However, the method for selecting electrons in one spin state instead of the other is not effective all of the time, and there are various depolarizing effects that the electrons experience on their way to the experimental hall. Due to this, the beam is not purely of one helicity state, so there is at best a partial polarization of the beam.

Several interactions can be used for determining the polarization of a beam of electrons, such as the Møller interaction, the Mott interaction, and the Compton interaction. All three methods are employed at various stages of the beamline at JLab, but in some instances certain interactions are more preferable than others. The Møller and Mott interactions, which are electron-electron scattering and electron-heavy atom scattering respectively, are both destructive because they require the usage of polarized targets (iron for Møller polarimetry, gold for Mott polarimetry)

that will destroy the beam, so while they can obtain a polarimetry measurement the beam is unable to be used for any other measurements. Because of this, the Compton interaction, or electron-photon scattering, is of interest for gathering a continuous polarimetry measurement while obtaining other measurements to find the main quantity of a particular experiment, since the beam is not completely destroyed in the process. [15]

In the experimental Hall A of JLab, the Compton polarimeter kinematically separates electrons that have experienced the Compton interaction from the rest of the beam. This allows for the translation of a spectrum of momenta to a spectrum of positions. A detector that can separate electron events by position is therefore necessary for a Compton polarimeter where the electrons are used to measure the polarization. In Hall A, a silicon strip detector is used to discern the position of the scattered electrons in space. The resulting analog signals are then translated into digital signals that contain the position information.

Due to noise in the experimental halls, the board that changes analog signals to digital signals needs to be replaced to compensate for this. One of the possible candidates for this is a board that was used in the Hall C polarimeter to process diamond detector signals called the QWEAK Amplifier-Discriminator, or QWAD. This board has an additional time-over-threshold capability that might be useful in the further filtering of noise, allowing us to discern events from noise by the duration of the logic signal.

To test this board, its functionalities as a self-contained unit were examined via a signal generator by monitoring the digital outputs. From there, a set of further

experiments were devised to test the QWAD in conjunction with a single plane of the silicon strip detector from JLab. These experiments would tell us if the QWAD would be useful as a way to digitize the position data from the electron detector.

Chapter 2

Theory and Motivation

Parity-violating electron scattering experiments, or experiments involving electron scattering processes that violate the symmetry of nature known as parity, are used to probe properties of nature via the weak interaction. These experiments require knowing the beam helicity state in order to make crucial corrections to any measurement obtained via such experiments. Therefore, we use Compton polarimetry to take the measurement concurrently with other measurements in the experiment. The electron detector used to obtain a beam polarization measurement was selected with the process of Compton polarimetry in mind.

2.1 Spin-Dependent Parity Violation

Polarimetry is used when experiments explore parity violation with interactions that are dependent on the spin state of the electron that enters the interaction. Since the spin state of the beam affects the outcome of scattering events in parity-violating electron scattering experiments, it is then necessary to have a measurement of that

overall spin state of the beam. To demonstrate how the spin state affects the outcome of scattering events via the weak interaction, we use the examples of PREX and CREX and the dependence on beam helicity to measure a scattering asymmetry.

2.1.1 Parity-Violating Electron Scattering

Parity is one of the fundamental symmetries of nature. Under the parity operator $\hat{P}$ if a vector quantity transforms as follows:

$$\hat{P}\begin{pmatrix} a \\ b \\ c \end{pmatrix} = -\begin{pmatrix} a \\ b \\ c \end{pmatrix},$$

parity is said to have been conserved with respect to that quantity.

With respect to the four fundamental forces, we see that parity is conserved in three of these interactions, the electromagnetic, gravitational, and strong interactions respectively. However, the weak interaction does not conserve parity. Because of this, it is said to be a parity-violating interaction. The parity violation enables us, therefore, to separate the weak interaction from other interactions in experiments. [13] [12]

Parity-violating electron scattering experiments rely on this violation of parity to sort weak interaction electron scatters from the more prevalent electromagnetic scatters that occur in a typical particle physics experiment which has charged particles. This is achieved via measuring scattering asymmetries of the form presented in equation 1.1. However, since we cannot measure scattering cross-sections directly, we instead begin obtaining an experimental asymmetry A_{exp} measurement in terms

of number of scattering events N for the two helicity states as:

$$A_{exp} = \frac{N_+ - N_-}{N_+ + N_-}. \tag{2.1}$$

Here, the helicity states h defined as (+) and (-) can be determined via:

$$h = \frac{\vec{s} \cdot \vec{p}}{|\vec{s} \cdot \vec{p}|}, \tag{2.2}$$

where $\vec{s}$ is the spin vector and $\vec{p}$ is the momentum of the particle.

2.1.2 The Weak Interaction

The weak interaction is one of the four fundamental interactions in physics. It occurs on subatomic scales, is mediated by the W and Z bosons, and also violates parity. This interaction has a spin-dependence, and is observed in parity-violating electron scattering experiments. [13]

Two examples of experiments that take advantage of the weak interaction to determine a particular quantity are the experiments PREX (Pb Radius EXperiment) and CREX (Ca Radius EXperiment) at JLab. Here electron scattering is used to determine the neutron radii for ^{208}Pb and ^{48}Ca, respectively. These radii are determined by finding which portion of the scattered electrons experienced the weak interaction like in figure 2.1 with the nuclei of the lead and calcium targets.

Electrons that experience the weak interaction are sorted from the electromagnetic by finding the scattering asymmetry between the two possible helicity states of the beam. [6] [7] This is also true for other scattering experiments that seek out parity-violating electron scattering events. Therefore, in order to separate these scattering processes from other processes we must know the overall beam helicity state. This is what necessitates polarimetry in experiments where parity violation is explored.

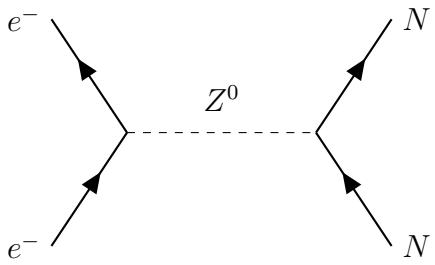

Figure 2.1: One of the possible interactions between a nucleus and an electron is a weak scattering process, which is parity-violating electron scattering. In this first-order representation of the weak interaction in the form of a Feynman diagram, a Z_0 boson is exchanged between the two subatomic bodies.

2.2 Compton Interaction

Compton polarimetry uses the Compton interaction, the interaction between electrons and photons, to determine the overall polarization of the beam. In order to obtain the beam polarization, it is necessary to understand the scattering behaviour.

2.2.1 Kinematics

Let us begin with a photon of energy k and an electron of energy E with a momentum p. In relativistic mechanics we model these quantities using four-vectors with index a which contain both the energy and momentum quantities. [10] Using this form, these quantities are defined on a general interaction plane such as the one defined in figure 2.2 as:

$$p^a = \begin{bmatrix} E \\ p\cos\beta \\ p\sin\beta\cos\psi \\ p\sin\beta\sin\psi \end{bmatrix}, k^a = \begin{bmatrix} k \\ k\cos(\alpha_c+\beta) \\ k\sin(\alpha_c+\beta)\cos\psi \\ k\sin(\alpha_c+\beta)\sin\psi \end{bmatrix}. \tag{2.3}$$

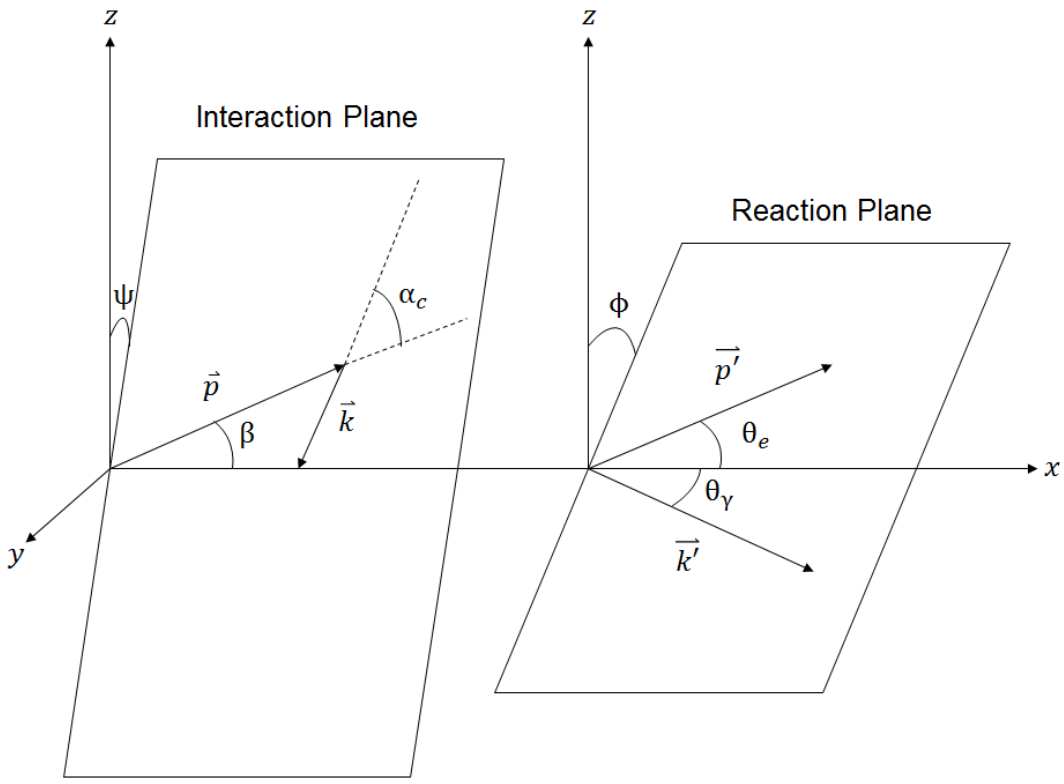

Figure 2.2: The Compton interaction and reaction planes as described in the section on kinematics. In general, the Compton interaction occurs on one plane, and the reaction plane is treated separately. Each of these planes are formed by the momentum vectors of the electron and photon respectively, and coordinates are defined in terms of the x, y, and z axes.

Here we define the angle β as the angle between the x-axis and the path of the electron, ψ is the angle of the plane with respect to the z-axis, and α_c is the angle of the path of the photon with respect to the path of the electron. We must also

consider the final energies (E', k') and momentum (p') on the reaction plane as:

$$p'^a = \begin{bmatrix} E' \\ p'\cos\theta_e \\ p'\sin\theta_e\cos\phi \\ -p'\sin\theta_e\cos\phi \end{bmatrix}, k'^a = \begin{bmatrix} k' \\ k'\cos\theta_\gamma \\ k'\sin\theta_\gamma\cos\phi \\ k'\sin\theta_\gamma\sin\phi \end{bmatrix}, \tag{2.4}$$

where we define ϕ as the angle of the reaction plane with respect to the z-axis, and the angles θ_e and θ_γ are the trajectory angles of the electron and the photon after the interaction respectively. Figure 2.2 shows an example interaction for the general case.

Let us now take this general case and consider where the interaction plane and the reaction plane are both the same, where $\psi = \phi = \frac{\pi}{2}$, and where the electron has initial momentum only along the x-axis ($\beta = 0$). This is the kinematics case that is experienced at Jefferson Lab's Compton polarimeter. Our four-vectors are then expressed as:

$$p^a = \begin{bmatrix} E \\ p \\ 0 \\ 0 \end{bmatrix}, k^a = \begin{bmatrix} k \\ -k\cos\alpha_c \\ -k\sin\alpha_c \\ 0 \end{bmatrix}, p'^a = \begin{bmatrix} E' \\ p'\cos\theta_e \\ p'\sin\theta_e \\ 0 \end{bmatrix}, k'^a = \begin{bmatrix} k' \\ k'\cos\theta_\gamma \\ k'\sin\theta_\gamma \\ 0 \end{bmatrix}. \tag{2.5}$$

Given this case, we show that the energy of the scattered photon can be expressed as:

$$k' = k\frac{E + p\cos\alpha_c}{E + k - p\cos\theta_\gamma + k\cos\alpha_c\cos\theta_\gamma}. \tag{2.6}$$

Furthermore, let us consider the limiting case where the crossing angle of the photon and the electron α_c is sufficiently small where we can approximate the crossing angle as zero. Let us also substitute a quantity $\gamma = E/m$ where m is the mass of the electron, so we can further simplify the energy as:

$$\frac{k'}{k} \simeq \frac{4a\gamma^2}{1 + a\theta_\gamma^2\gamma^2}, \tag{2.7}$$

where

$$a = \frac{1}{1 + \frac{4k\gamma}{m}} = \frac{1}{1 + \frac{4kE}{m^2}}. \tag{2.8}$$

The energy and momentum of the electron can also be obtained via conservation of four-momentum.

Let us now consider the case where the photon that is scattered in the Compton interaction has the maximum energy that a photon could possess after experiencing scattering. In the definition given by equation 2.8, we adjust the quantity of θ_γ to have a value of zero, or to state that the photon scatters in such a way that it goes along the same path as the electron did. This gives us that the maximum energy of the photon as:

$$k'_{max} = 4ak\gamma^2 = 4ak\frac{E^2}{m^2}. \tag{2.9}$$

We must know the maximum energy of the photon so that we can obtain mathematical definitions that are expressed in terms of this energy and to also take into account the range of allowed electron energies which will be used to motivate the design of the electron detector.

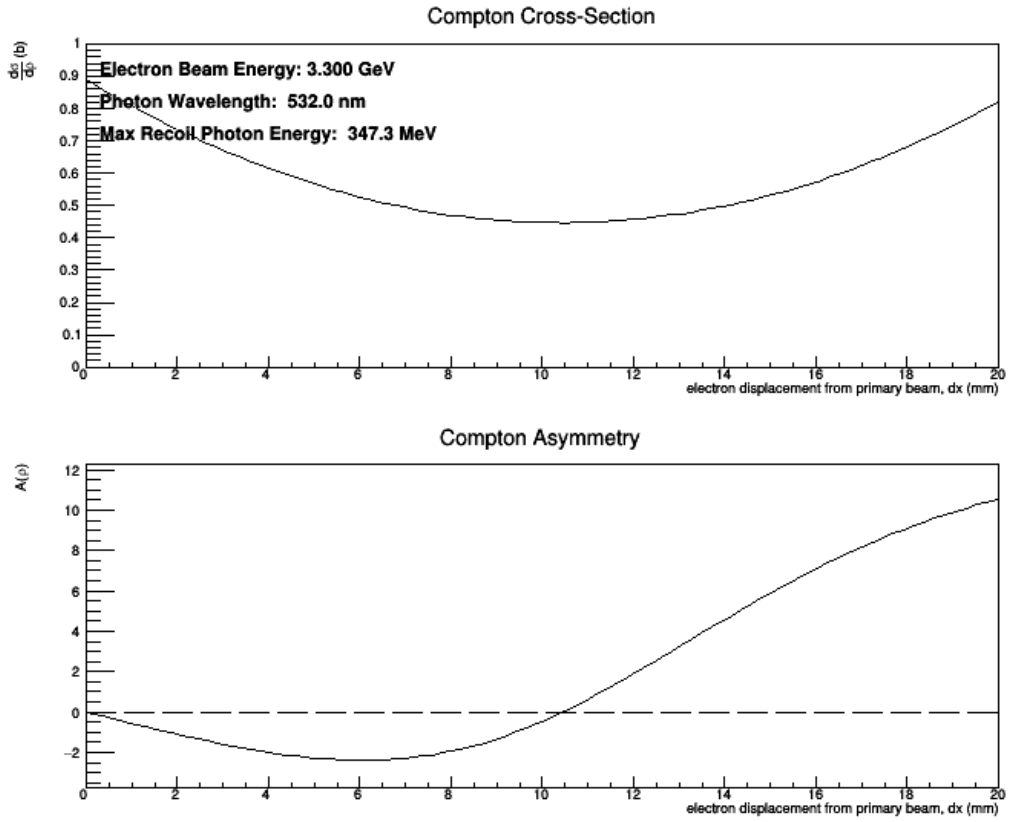

Figure 2.3: Here is an example of the Compton cross-section and the Compton asymmetry calculated for a range of ρ that are theoretically obtained using a beam energy of 3.3GeV, a photon wavelength of 532.0nm, and a maximum photon energy k'_{max} of 347.3MeV. The electron displacement from the beam forms the x-axis, and allows us to predict what values would be measured by an electron detector that can measure over those distances.

2.2.2 Cross-Section and Asymmetry of Polarized Compton Interaction

Let us define the differential cross section of the polarized Compton interaction. Here we define the angle ψ as the angle of the spin of the electron with respect to the z-axis, and the angle ϕ is defined as the azimuthal angle of the photon on the plane perpendicular to the interaction plane. The electron beam's polarization is defined as P_e, and the circular polarization of the photon as chosen via a circular polarizer

is defined as P_γ. Given these quantities, the polarized cross-section for the Compton interaction is given by:

$$\frac{d^2\sigma}{d\rho d\phi} = \frac{d^2\sigma_0}{d\rho d\phi} \mp P_e P_\gamma \left(\cos\psi \frac{d^2\sigma_1}{d\rho d\phi} + \sin\psi \cos\phi \frac{d^2\sigma_2}{d\rho d\phi} \right). \tag{2.10}$$

Where three sigma terms are defined as:

$$\frac{d^2\sigma_0}{d\rho d\phi} = r_0^2 a \left[\frac{(\rho(1-a))^2}{1-\rho(1-a)} + 1 + \left(\frac{1-\rho(1+a)}{1-\rho(1-a)} \right)^2 \right]$$

$$\frac{d^2\sigma_1}{d\rho d\phi} = r_0^2 a \left[(1-\rho(1+a)) \left(1 - \frac{1}{1-\rho(1-a)} \right)^2 \right]$$

$$\frac{d^2\sigma_2}{d\rho d\phi} = r_0^2 a \left[\rho(1-a) \frac{\sqrt{4a\rho(1-\rho)}}{1-\rho(1-a)} \right].$$

[10]

Within these three definitions, we use r_0 to represent the classical electron radius, the quantity a is still the one from equation 2.8, and we define a new physical parameter ρ as:

$$\rho = \frac{k'}{k'_{max}}. \tag{2.11}$$

For each of the sigma terms, σ_0 is the unpolarized cross-section of the Compton interaction, σ_1 is the longitudinal polarized component, and σ_2 is the transverse polarized component [10].

Since the momenta of the electron and photon are confined to the plane of interaction where the laser crosses the electron beam and both are parallel to the x-y plane as shown in the previous section, we can ignore all contributions for any scattering events where $\psi \neq 0$. Upon integrating over the angle ϕ this simplifies our

cross-section as:

$$\frac{d\sigma}{d\rho} = \frac{d\sigma_0}{d\rho} \mp P_e P_\gamma \frac{d\sigma_1}{d\rho}. \tag{2.12}$$

where we can think of the second term as an asymmetry depending on the helicity states of the photons and electrons that are experiencing the Compton interaction.

Given this way to compute the cross section, we then move on to the scattering asymmetry. The longitudinal asymmetry of the beam A_l can be computed as:

$$A_l = \frac{\sigma^{\rightarrow}_{\Rightarrow} - \sigma^{\leftarrow}_{\Rightarrow}}{\sigma^{\rightarrow}_{\Rightarrow} + \sigma^{\leftarrow}_{\Rightarrow}}, \tag{2.13}$$

where $\sigma^{\rightarrow}_{\Rightarrow}$ is the cross-section for where the electrons and photons are polarized parallel and $\sigma^{\leftarrow}_{\Rightarrow}$ the cross-section for anti-parallel polarizations [11].

Experimentally, we obtain the asymmetry by looking at the rates N of events with particular energies, and comparing the two for differing helicity states. These rates are defined by looking at individual ρ, which can be thought of as individual bins for counts in a histogram. We define the experimental asymmetry at individual ρ as:

$$A_{exp} = \frac{N^+(\rho) - N^-(\rho)}{N^+(\rho) + N^-(\rho)}, \tag{2.14}$$

where the (+) and (-) signs represent the overall helicity state of the beam, which corresponds to the directions of the spin and momentum shown in equation 2.13. An example of a scattering asymmetry and a cross-section calculated in terms of ρ can be found in figure 2.3.

This experimental asymmetry is related to the polarizations, scattering cross section terms, and the theoretical longitutinal asymmetry as follows:

$$A_{exp} = -P_e P_\gamma \frac{d\sigma_0/d\rho}{d\sigma_1/d\rho} = P_e P_\gamma A_l \tag{2.15}$$

When we finally determine the asymmetry of the Compton interaction, this leads us to be able to determine the overall beam polarization as:

$$P_e = \frac{A_{exp}}{P_\gamma A_l}. \tag{2.16}$$

2.2.3 Compton Polarimeter

At JLab's Hall A the Compton Polarimeter is placed near the beam's entrance into the experimental hall. The beamline is first lowered below the beamline's usual path into the hall via two magnetic dipoles. From there, the beam is brought to an interaction region where it crosses paths with a circularly polarized laser in a Fabry-Pérot cavity, or a space where a laser is kept in a cavity by way of reflection between two parallel mirrors. Then, a second set of magnetic dipoles lift the beam back into the main beamline. Figure 2.4 shows the Compton Polarimeter assembly.

Scattered electrons are moved into the path of a silicon plane detector which can be used to discern the distance of the electron above the beamline and allows us to obtain a momentum spectrum in terms of this relative distance. For examining the scattered photon there is a photon calorimeter, which is a scintillator that is placed below the fourth dipole. It is directly in the path of the scattered photons, and allows for capturing an energy spectrum of Compton events. These measurements are integrated over a "helicity window," where one helicity state is preffered over the other by the beamline injector at JLab.

Measurements integrated over each of these helicity windows allow us to obtain a clearer picture of the overall asymmetry and cross section of the Compton scattered electrons. This reduces the overall systematic error due to the limitations of the two

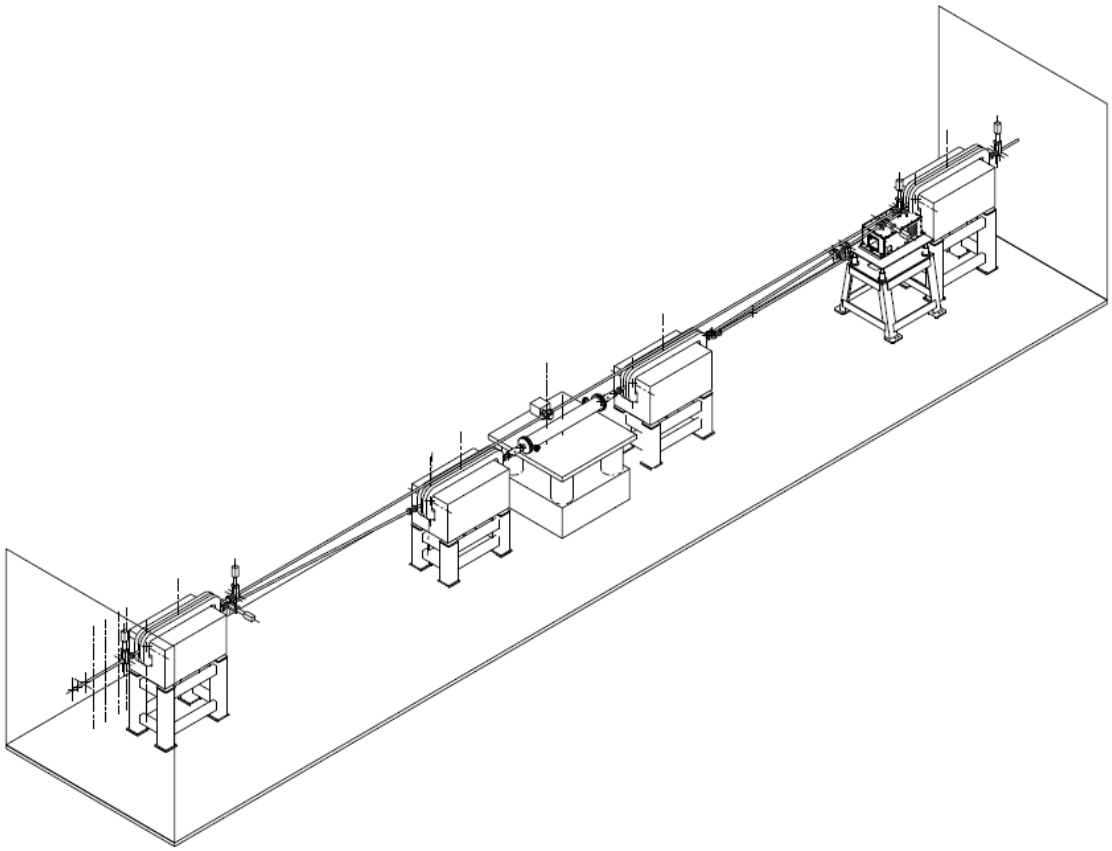

Figure 2.4: Compton chicane as shown in a design proposal. Four magnetic dipoles bring the main beam into an interaction area and back to the main path of the beam. An interaction table with a Fabry-Pérot cavity houses the circularly polarized laser which interacts with some of the electrons. Two detectors for detecting the scattered electrons and photons are used to obtain the measurement in conjunction with each other. Courtesy of US Dept of Energy's Jefferson Lab

detectors. [8]

2.3 Electron Detector Operation

The Compton chicane sorts out the momenta of the particles via bending their path in a magnetic field, so in order to detect the momenta, the detector must be able to resolve position relative to the main beamline. The Compton polarimeter at Jefferson

Lab achieves this via arranging semiconductor active areas on the detector in strips that are placed perpendicular to the main beamline. Charges in semiconductors with a constant voltage applied across the expanse can produce an electronic signal when charged particles pass through them with sufficiently high energy, and this lets us use them for the detection of charged particles.

2.3.1 Measuring Scattered Electron Momentum

It is known that for a particle with a charge q and mass m passing through a uniform magnetic field of strength $\vec{B}$ with a relativistic momentum $\vec{p}_e$, the force (expressed here as the change of momentum $\vec{p}$ with respect to time t) that is experienced by the particle is:

$$\frac{d\vec{p}}{dt} = \frac{q\vec{p}_e}{cm} \times \vec{B}. \tag{2.17}$$

We can simplify the momentum by saying it is purely in the x-direction and that the field from the magnetic dipole is completely orthogonal to the path of the particle in the y-direction. The charge of each electron is the elementary charge, $-e$. When we evaluate the cross-product above, we obtain:

$$\frac{d\vec{p}}{dt} = \left(0, 0, \frac{ep_eB}{cm}\right). \tag{2.18}$$

Which describes a circular path [4] [5].

Due to this property of charged particles moving in uniform magnetic fields, we can use the position of the charged particle as it leaves the magnetic field as a way to determine its momentum. Since the path of a charged particle in this situation is circular, it is straightforward to obtain the radius of the circular path that it would travel in a uniform magnetic field big enough to contain the entirety of the circular

path. This radius, R, can be expressed with:

$$R = \frac{p_e}{eB}. \tag{2.19}$$

We note that in the above equation that R is directly proportional to the momentum of the electron, meaning that for the radius of curvature of an electron that experienced a collision and now has a new momentum of p'_e, we obtain:

$$R' = \frac{p'_e}{eB}. \tag{2.20}$$

This radius R' will always be smaller so long as the magnetic field strength B remains the same throughout, as is expected of the magnetic field in the chicane.

Let us now have a region with a uniform magnetic field, and then define the distance along the z-axis that the particle travels while in this field region as d. We can construct a trapezoid where one side is the length of the uniform magnetic field and the second side of length d are placed perpendicular to each other, and the other two sides are one radius of length R' as defined above placed parallel to d, and another radius completing the trapezoid with an angle θ with respect to the other side of length R'. By using geometric arguments we find the distance that the particle travels along the z-axis in this region to be:

$$d = R'(1 - \cos\theta). \tag{2.21}$$

This displacement can be measured and used to determine the momentum of the particle through the value of R' that is obtained. However, with the way the magnetic chicane is set up it is not practical to place a detector right at the magnetic dipole exit where the uniform magnetic field ends. We instead place the detector further

down the beamline at a position ℓ along the x-axis, giving the scattered electrons more time to spread away from the main beamline. By doing this, we must introduce a second term to determine the overall vertical displacement from the beamline, D, as follows:

$$D = \ell \tan\theta + R'(1 - \cos\theta). \tag{2.22}$$

Figure 2.5 shows this displacement in the context of the proposed design of the Compton polarimeter at JLab's Hall A.

It can be shown that the triangle formed by the x and z positions of the electron detector is similar to a triangular section in the trapezoidal region that we used to obtain the initial veritical displacement term, so this gives us a straightforward way to obtain θ for a measurement. If we take multiple planes, place them in parallel to each other, and then place them perpendicularly to the chicane pipe, and by extension the beamline, we can by determining which positions in the detector an electron goes through the angle θ that it has from leaving the magnetic field region. If we can also track the vertical position of the detector and the location of the beamline via beam monitors, we can directly measure the quantity D as well. This gives us a detector design that can allow us to find R', and therefore the momentum p'_e with:

$$p'_e = eB\frac{D - \ell\tan\theta}{1 - \cos\theta}. \tag{2.23}$$

Keeping all these considerations in mind, any detector that is used to determine the momentum spectra of the Compton interaction must also be capable of resolving the position of the electron as it tracks through the stages of the detector. The placement of multiple planes in parallel is essential for the determination of the angle

of departure from the dipole field. Being able to divide up the detector into multiple active areas to have resolution of position is also essential for determining the overall vertical displacement of each individual electron. This motivates our detector design by introducing the need to be able to resolve events by position relative to the beamline after it travels through the magnetic chicane. In the detector at JLab, this results in us using a series of four planar detectors in parallel to the beam, and with the active areas divided into areas of 198 strips each. By tracking which of the strips the electron traverses, we can then determine the electron's height above the beamline and, by extension, its momentum. [8]

2.3.2 Semiconductor Detector Principles of Operation

All semiconductors have a band structure that consists of a valence band and a conduction band, which can be exploited in electronics for various purposes. When ionizing radiation moves through an space filled with a semiconducting material, local charged particles get displaced as the particle traverses the medium and also gain energy that lets a portion of the charged particles enter certain energy states within the band structure of the material. In semiconductors, this will be the conduction band, and any currents that result from the displacement of charged particles into the conduction band allow us to acquire a signal that can be used to see if a particle has traversed the medium.

When a semiconducting material has an electric field applied across the medium as in figure 2.6, this allows for charges in the conduction band to move from one direction to the other. The current that results from this motion of charges is what

can be measuredl. This type of detector is also less susceptible to backgrounds caused by gamma radiation, so this makes semiconductor detectors ideal for our application.

Two potential choices in material that we have for constructing the detectors are silicon and diamond. Both materials have been used in Compton polarimeter electron detectors at JLab. Silicon is used presently in Hall A. The signal size is large compared to diamond, but the radiation hardness is less than that of diamond. The silicon strip detector in Hall A is split up into 198

After ionizing radiation passes through the semiconductor and the signal is picked up, the signal can go through one or more amplification and discrimination stages to sort events caused by particles that pass through the detector from the noise. One such example of an amplifier/discriminator board is the QWAD.

2.3.3 QWAD

The QWAD is a collection of circuitry, shown in figure 2.7, that converts the signals from a strip detector into a set of digital on/off signals that can be used to take analog signals and render them into digital position data with the aid of a scalar.

+5V and -5V voltages are used to power the QWAD, and these are applied to two terminals on a connector that is built into the board. The remaining connections of the connector are set to ground, or the third pin also has a voltage level applied to it if the external threshold mode is selected.

A semiconductor strip detector is connected to the QWAD, which allows for the instrumentation of a quarter of its strips. Specifically for the semiconductor detector used at JLab, the QWAD can only instrument 48 of the strips at a time. These

48 strips are then further paired up with three digital signal channel banks, each with 16 LVDS, or Low-Voltage Differential Signalling, outputs that correspond to a particular strip on the detector. This is a method of outputting digital signals that should reduce noise Then, the signals go through an amplification stage that consists of several transistor-based amplifiers. The signals are both increased in amplitude and elongated in time. This allows for the utilization of two criterion for determining if an event is an actual hit on the electron detector: the threshold voltage used for filtering the amplified signals, and the length of time that the signal persists over the threshold.

Each of the channels is attached to a comparator that allows us to filter for the first of these critera: threshold voltage. The signal is first sent along two separate comparator channels, with one of them having a variable resistance detailed in the next paragraph. That variable resistance is what allows for the QWAD to have a threshold setting for the voltage. Then, the comparator outputs an LVDS signal which lasts for as long as the amplified input signal remains above the threshold voltage. A circuit diagram for the QWAD channels is shown in figure 2.8.

There are two threshold modes, the first is an internal threshold mode that is formed by a voltage divider along one of the terminals of the comparator. The voltage divider formed by the potentiometer, when the potentiometer is set to its maximum resistance of 100Ω draws a total current of:

$$I_{Comparator} = \frac{5V}{4550\Omega} \approx 0.0011A. \tag{2.24}$$

This internal mode allows us to achieve a range of default internal voltage threshold adjustments of up to approximately 0.11V at the maximum setting of the potentiome-

ter. For the diamond strip detectors which have smaller output voltages initially, this works well. The second of the threshold modes is an externally set threshold mode that can be adjusted using the third pin of the MOLEX connector through which the QWAD is powered.

There is also a calibration input on the QWAD that first passes through a simple voltage divider before it is then passed on to each of the individual channels. The maximum voltage that can be applied here is 10.0mV. This can be used to test the functionality of the QWAD without having to plug in the outputs from a strip detector and to also calibrate the thresholds in the absence of such a set of signals as well.

The end result of this setup is a system that possesses the capability to produce a digital signal that lasts a proportional length of time to the time a signal remains higher than the threshold voltage. This capability can be used in Compton polarimetry in order to interpret the position data that are given by analog signals from a strip detector. Given the correct hardware and software working in combination with each other, the QWAD can be a powerful tool. [9]

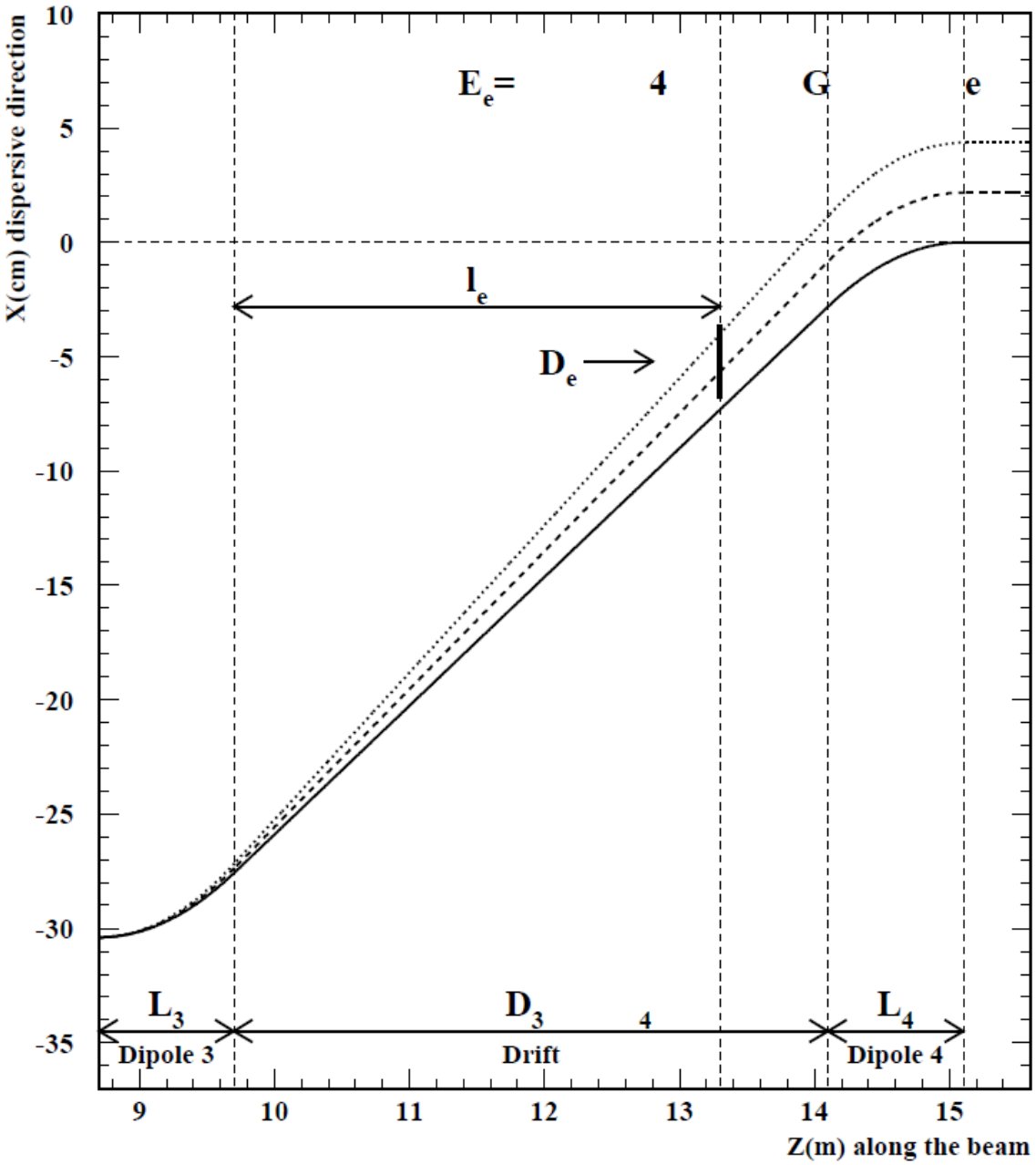

Figure 2.5: Electrons are displaced by moving through the magnetic dipoles. In this figure, D_e is equivalent to D, and l_e is dequivalent to ℓ_e as described in this section. The axes represent the distance along the beamline and the dispersive direction and scaled appropriately. A thick black line placed at D_e represents the position of the electron detector, which captures the range of scattered electrons for this particular energy level given. Courtesy of US Dept of Energy's Jefferson Lab

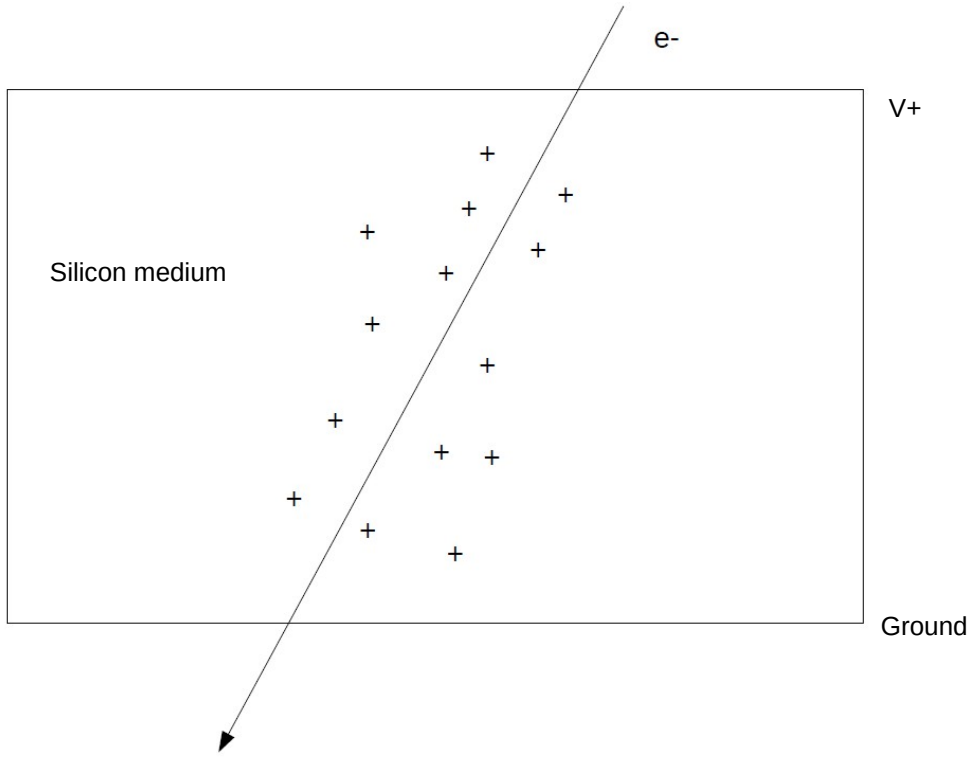

Figure 2.6: A semiconductor detector works by ionizing radiation, such as an electron, displacing charges in a semiconducting medium that has a voltage applied across it. An electron with negative charge with sufficiently high velocity temporarily creates a region of positive charge, which is quickly filled and causes an electric current to happen.

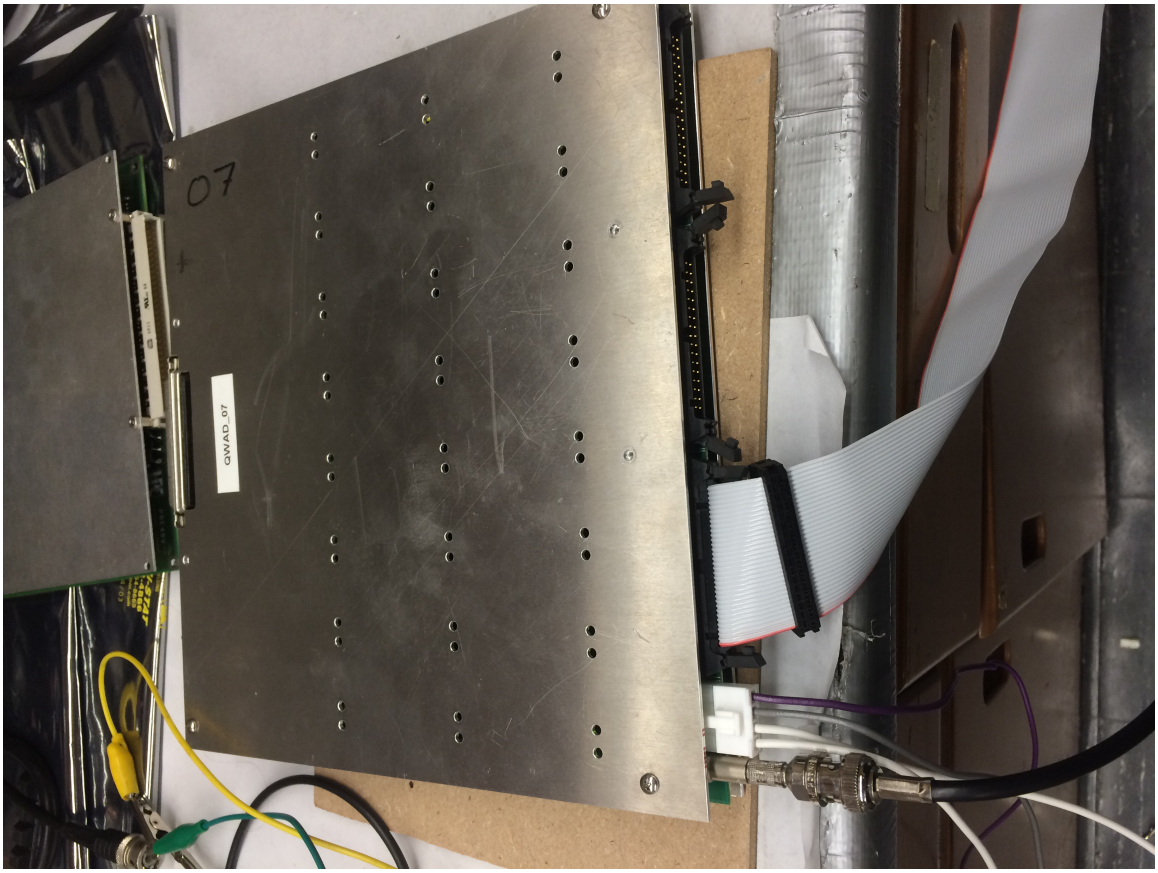

Figure 2.7: The QWAD Board shown above is set up in a pulse testing mode. From the bottom right, a BNC connector is used to send a test signal to a calibration line that simulates all channels at once, a connector above that is used to provide power and external threshold voltage, and a ribbon cable above that is used to connect the QWAD to a scaler.

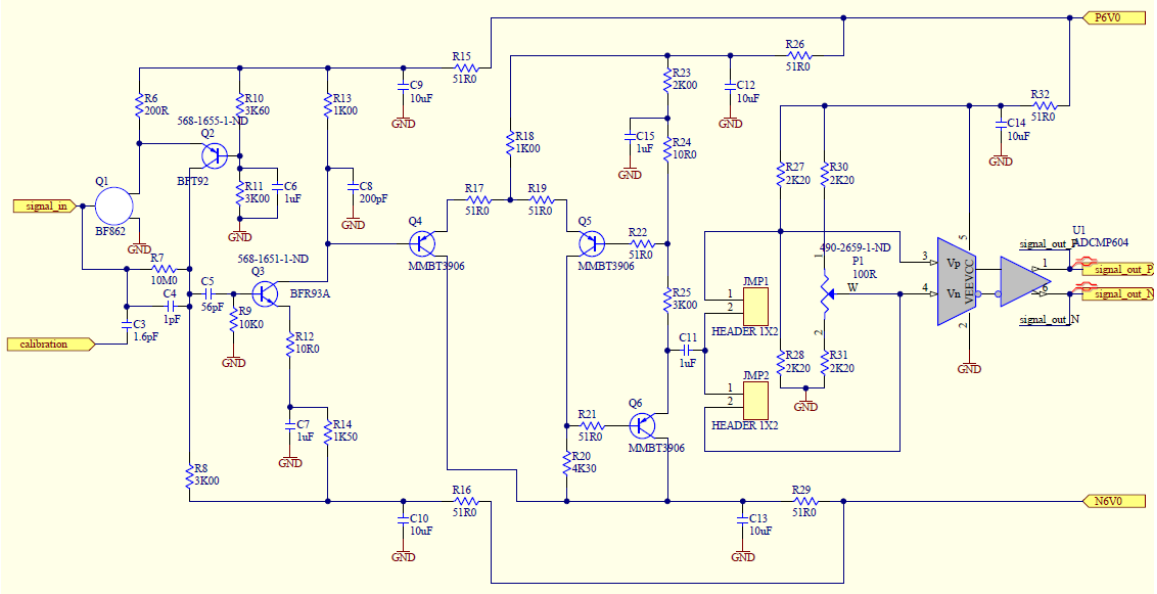

Figure 2.8: Each channel of the QWAD had two stages, both of which are shown in the above circuit diagram. First, a signlal from either the calibration line or a channel of the strip detector arrives at an amplification stage, made up of a differential amplifier among other amplification circuits. The effect of this is to both amplify and elongate any signals from the silicon strip detector. After that, it passes through a discriminator stage which converts it into a digital signal. Courtesy of US Dept of Energy's Jefferson Lab

Chapter 3

Methodology

Testing the QWAD in conjunction with the silicon strip detector from JLab involved several tests. First, we evaluated the QWAD's own signal responses via a series of calibration line tests. Finally, through digital rate tests with a source, we can evaluate the overall potential that the QWAD has to work in conjunction with the silicon strip detector.

3.1 Rate, Threshold

The QWAD was calibrated using a dedicated channel, and a function generator was used to test the LVDS response. During this calibration process, a variety of pulse tests, the details of which are expanded upon in this section, were performed to gauge the performance of the QWAD and to understand which features to use. [9]

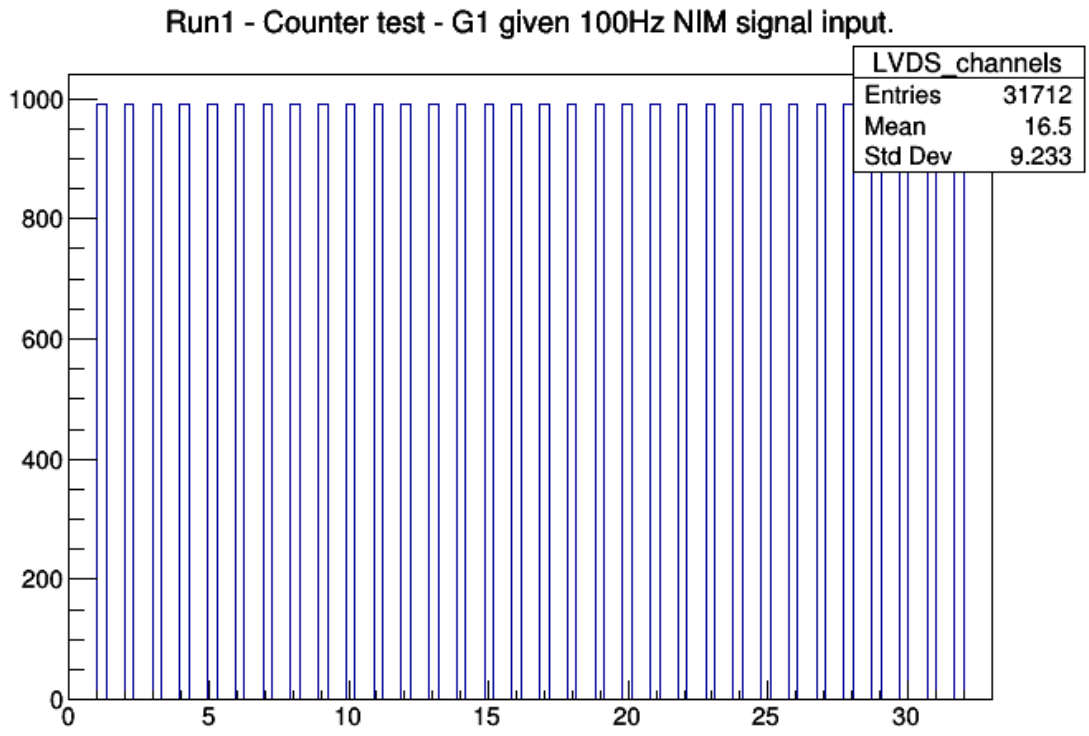

Figure 3.1: A preliminary test of the V1495 scaler where the channels were tested with the test signal mode of input G1. We expected 1000 events to be gathered on each of these channels, and this automated histogram from ROOT showed that this is what happened, uniformly, across all channels. This shows that the scaler doesn't contribute to the error.

3.1.1 Rate Tests

In order to test the QWAD, pulse generators were used. Each of these had the ability to adjust the amplitude, frequency, and duration of the pulses. A TTL (Transistor Transition Logic) level synch output was also available, which could be used as a trigger signal if translated to the proper logic voltage levels for our apparati. Most of the time, only a single pulse generator was used in the experiment. However, since it would be useful to have moments where the rate of the trigger signal could be varied

independently of the main pulse signal, there were tests where two pulse generators were used at once.

To acquire the total amount of counts from the QWAD a V1495 general multipurpose VME board with the FW1495SC multievent scaler firmware loaded onto it was used. A scaler is a This board had 64 LVDS channels available as inputs, and two NIM (Nuclear Instrumentation Module) logic level-based inputs that allowed for triggers to be accepted and to access other functionalities. NIM is the standard output for most nuclear instrumentation modules, including hardware that would be used in any experiments testing our detector. The first of the NIM inputs, G0, was used exclusively to accept event triggers. The second of the NIM inputs, G1, could be used to access three functionalities: stopping the LVDS counters from accepting counts after the trigger gate ends, using a test signal to evaluate all the LVDS counters and their performance as in figure 3.1, and to reset the values of the counters. These logic behaviours are demonstrated in figure 3.2. Only the first two capabilities were used. In order to translate the TTL-level outputs from the pulse generator synch outputs so that they could be used in conjunction with the V1495, a logic translation unit was used to translate TTL levels to NIM levels.

Scope traces were obtained to evaluate the functionality of the calibration line and the LVDS comparators. This information was potentially useful for the purpose of timing and also for determining the proper orientation of the ribbon cable used to attach the QWAD to the V1495. Various other scope traces were used to obtain a picture of the noise levels that were present.

The V1495 counters were tested using the optional capability of the G1 input to

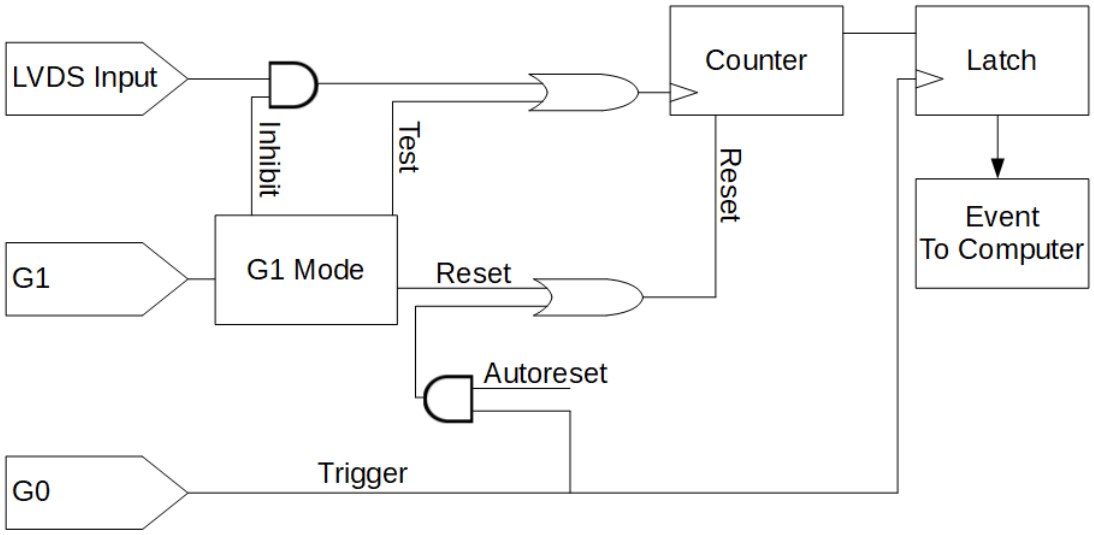

Figure 3.2: This is the logic diagram for the V1495 when the scaler firmware was loaded on it for the G1 and G0 inputs with respect to each LVDS channel. Not pictured is how the LVDS inputs connect to the counter directly. The inhibit mode keeps the counters from counting, the test mode increases counts on the counter independent of what the LVDS input does, and the reset mode allows for the counters to be reset from G1. Otherwise, the Autoreset mode can be turned on to allow the counters to reset from a trigger coming from G0. Each trigger activates the latch, which stores the current counting state and then sends the previous one off to the event buffer where it is read in by the computer [16].

test the capability of all the counters at once. A 100Hz NIM sinal was used to provide the trigger source for all of these particular tests. A second NIM signal was sent to G1 with varying rates. The purpose of this test was to see that the number of triggers that was expected were also counted. The connectivity of the QWAD and the V1495 were then tested by checking the orientation of the ribbon cable used. After that, we tested some other aspects of the QWAD's response.

Noise control tests were done to determine if there were any sources of noise that were contributing to the counts of events. One of the conditions tested was what

would happen if the signal generator was not plugged in versus plugged in and giving no pulse signal to the QWAD.

With the calibration line, three separate types of tests were performed. The first of these was a series of pulse tests that varied certain aspects of the pulses each time allowing us to see what effects this would have on the QWAD response. An example of the QWAD response to a pulse test can be seen in figure 3.3 The second of these were noise control tests, to see what happens if the QWAD is just left to operate by itself without having any inputs coming in.

Via the pulse tests, we found that the QWAD had quite a few noise issues operating by itself, and the control tests to establish the potential source of noise were necessary to isolate the problem. As the voltage of the signal given to the calibration line was lowered, the average number of counts in each channel decreased. As the frequency of both the signal, the calibration line signal, and the trigger signal were the same, the average number of events on each channel also remained the same up to 5kHz which was close to the maximum rate possible given the duration of the pulse selected. Having a higher trigger rate lead to undersampling of the events. The shortest possible pulse duration of 10μs still registered as an event with the QWAD's circuitry.

3.1.2 Threshold Tests

Our last set of tests was to examine the external threshold functionality.We first started with using the internal threshold modes to see if there was a minimum length of time that a signal had to spend over the threshold in order to register as events. This was achieved via modifying the pulse widths, and then checking the corresponding

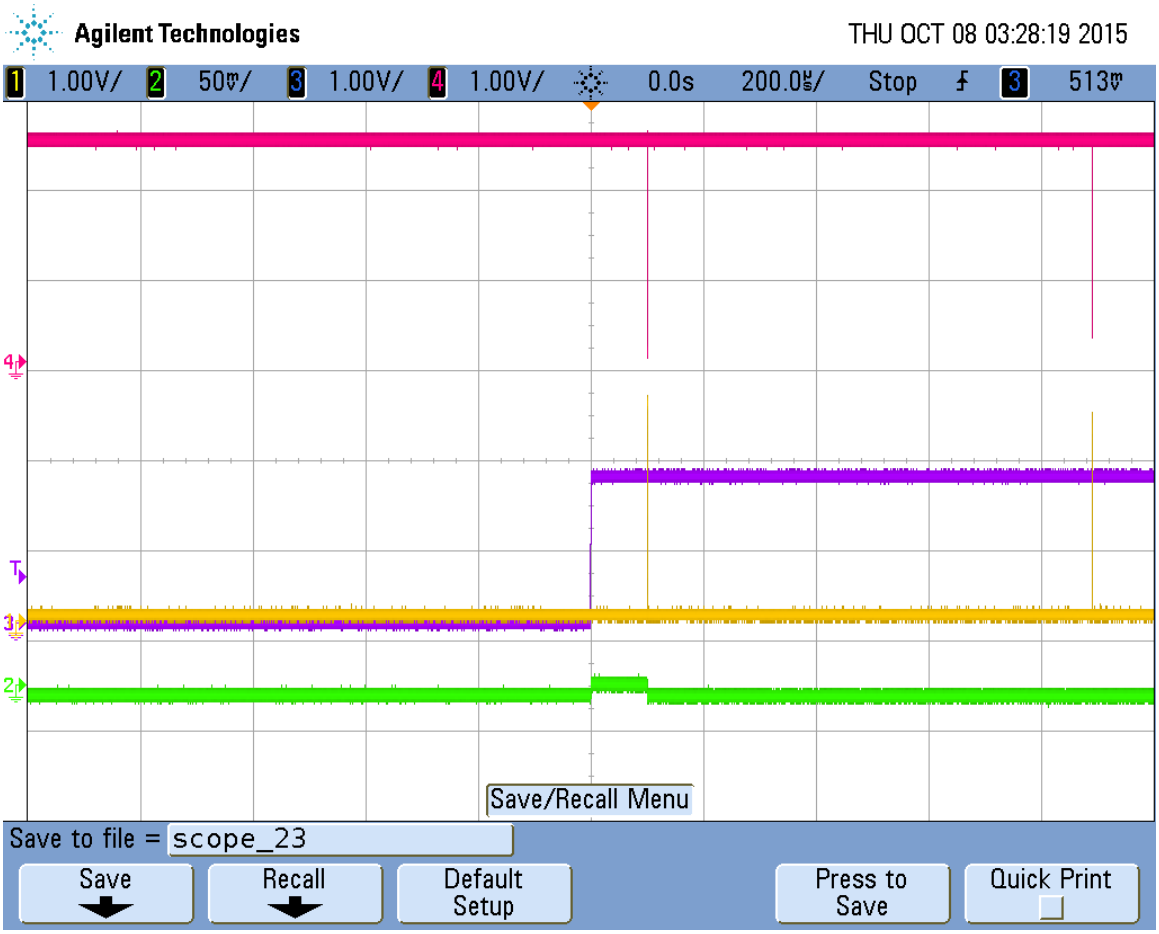

Figure 3.3: The QWAD's response to a pulse signal. Channel 2 is the pulse signal that was generated by a pulse generator, channels 1 and 4 are the LVDS response, and channel 3 is the trigger signal that was sent to the scaler module that was also generated by the same pulse generator. LVDS signals work by taking the difference between two voltage states and using that to determine digital on and digital off, so both had to be evaluated at the same time to check that it was functioning correctly.

digital output.

The next condition tested for was whether or not the QWAD was on or off. If the QWAD was powered on, the threshold modes were varied between the externally controlled threshold and the internally set threshold. For the externally controlled threshold, the threshold voltages of 6.7V and 7.7V were used. A 100Hz trigger signal

was sent to the V1495 for these tests.

The external threshold function was examined via applying a variety of voltages to the third MOLEX pin. The first set of tests varied this voltage in steps of 1.0V, and the second set of these tests varied it in steps of 0.1V. This voltage was applied by another power supply that was separate from the main power supply that was powering on the QWAD.

Varying the external threshold revealed that the lower the externally applied threshold, the higher the noise levels. This showed to us that the QWAD's externally controlled threshold feature worked as expected. By incrementing in steps of 0.1V, it was shown that a candidate for the best available external threshold voltage for these pulse tests was 6.7V. However, the noise was not completely eliminated at any threshold level, nor did the threshold levels offered to us by this mode allow us to cut off the , leading us to consider not using this threshold mode for the tests of the QWAD board that use the silicon strip detector.

Once the external threshold was explored, a few tests were performed in conjunction with the silicon strip detector to determine a way to adapt the internal threshold settings to best function with it. It was found that the best method of adjusting the internal thresholds was to apply a constant DC voltage in the range of 2.4V to 2.8V directly to a pin that corresponded to one of the comparators as shown in figure 3.4. This allowed us to use the internal threshold settings in conjunction with the silicon strip detectoron a single strip.

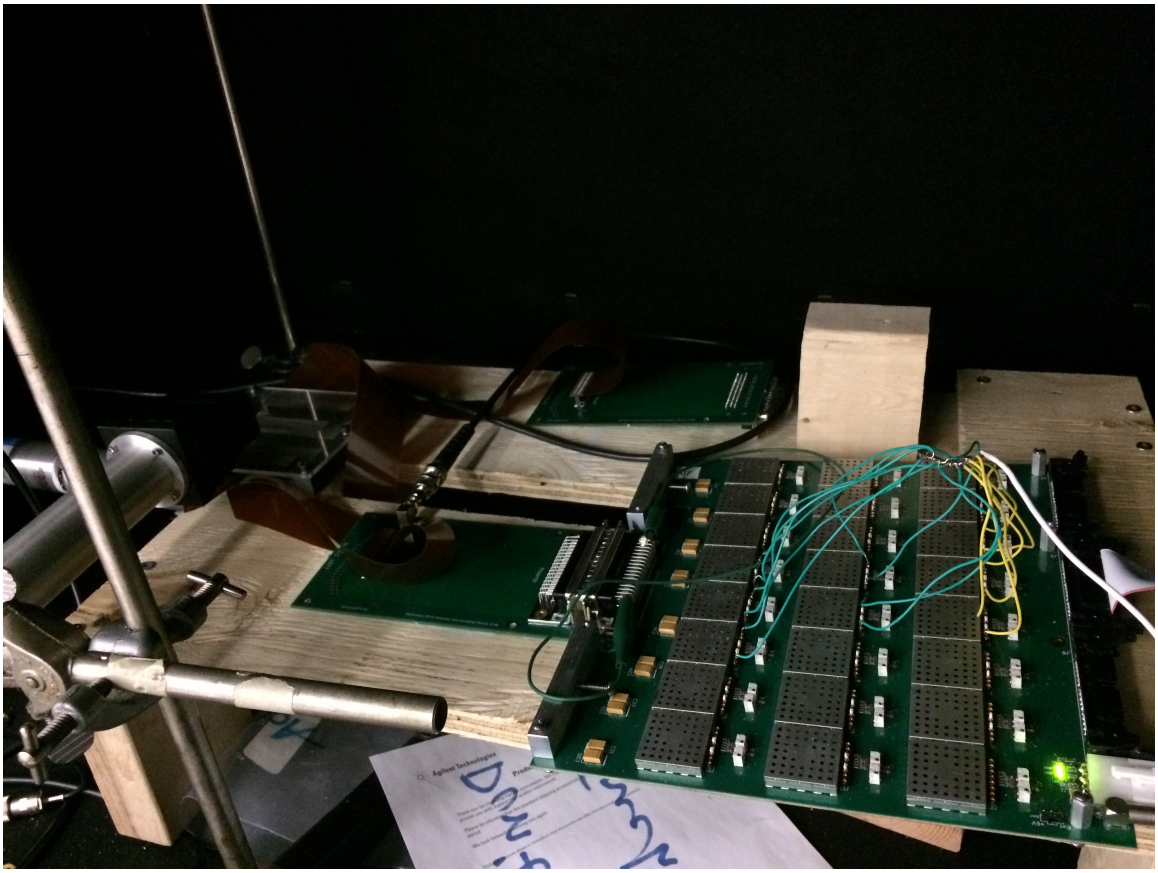

Figure 3.4: In this picture, the solution employed to modify the threshold of the QWAD outside of the ranges allowed by the potentiometers is shown. On the left of the pciture the detector is in its housing, and is connected to a breakout board by a ribbon cable. This breakout board was connected to the QWAD. On the QWAD, each pair of channels are housed in a metal housing with a few points of contact that allow for monitoring of signals and the application of external thresholds. A cable applied a constant DC voltage to each of the channels that were instrumented. A ribbon cable on the right side of the picture sent the LVDS signal to the scaler.

3.1.3 QWAD Modifications

Since there are different signal characteristics that the silicon detector exhibits in comparison to the diamond detectors that it was designed to work for, we had to make some adjustments. In order to make the QWAD work in conjunction with the silicon detector, it must experience one of two different modifications in order to use

the internal threshold mode of the QWAD board.

One of the first approaches we could have taken was to replace the potentiometers. As detailed in equation 2.24, the potentiometer connected next to the compators allows for variations of voltage up to approximately 0.11V with a current of approximately 0.0011A. As can be seen with the signal response, this is not a sufficient enough variation in voltage to allow for usage of the internal threshold mode of the QWAD board. For our purposes, we would like to augment the capability of the potentiometers. The voltage divider created by the QWAD's potentiometer, in order to accomodate the resolution of threshold necessary to discriminate between the noise and the signal would need to contain a potentiometer with a resistance $R_{Potentiometer}$ of at least 1kΩ.

By replacing the potentiometers with an $R_{Potentiometer}$ of 1kΩ, we can achieve the swings in voltage necessary to filter the noise from the signal. To show this we compute the current similar to the computation in equation 2.24:

$$I_{Difference} = \frac{5V}{5450\Omega} \approx 0.0009A. \tag{3.1}$$

Using this calculation, we find that if we replace the 100Ω potentiometer with a 1kΩ potentiometer that the voltage difference across the entire potentiometer becomes approximately 0.9V with this setup. The difference between the signal and the noise in the calculation is on the order of tenths of volts. Since a 1kΩ potentiometer has a range of approximately 0.9V that it can vary over, this easily would accomodate our needs. However, since drastic modifications to the QWAD board were out of the question chose a different approach.

The other approach that was used was applying a uniform voltage directly to the

comparators in order to adjust the internally set threshold. In this approach, instead of replacing the physical potentiometers, we just leave the potentiometers at the levels they were at and then just applied various voltage levels to a header pin that was directly connected to the terminal of the potentiometer that is used to set the internal threshold. Each channel was tested, and a voltage ranging from 2.7V to 2.9V was applied until the only LVDS signals that remained were ones due to events caused by ionizing radiation, and the particular voltage at the moment of cut-off for each channel are shown in table 3.1. The applied voltages were sufficiently similar enough for each channel that we could apply the same voltage to each of the channels.

Further information about the QWAD and its responses can be found in Appendix A.

3.2 The Experimental Setup

For testing the detector's operation in conjunction with the QWAD, a setup that uses one or more scintillator paddles with the silicon strip detector to look for coincidences due to radioactive decay products and cosmic rays was used. Several configurations of detectors were pursued, but a configuration that used a two-scintillator trigger with the source placed on top was pursued. Upon connecting the parts of the test bench together, it was essential to read them through a DAQ, or Data AcQuisition system. Because of this, the timing of the signals was important to keep in mind. [14]

Channel	Threshold Voltage
1	2.785V
2	2.736V
3	2.804V
4	2.757V
5	2.772V
6	2.714V
7	2.833V
8	2.822V
9	2.880V
10	2.778V
11	2.801V
12	2.786V
13	n/a
14	2.812V
15	2.746V
16	2.829V

Table 3.1: These are the threshold voltages for each of the channels connected to the centre channel bank of the QWAD where noise stopped giving a digital response. Since each of these are close to each other, for testing purposes we can apply the same voltage across channels while doing a threshold scan of the QWAD.

3.2.1 Test Bench Design

The detectors must be positioned and powered correctly, and any respective housings and peripheral attachments must be taken into consideration. The DAQ must be

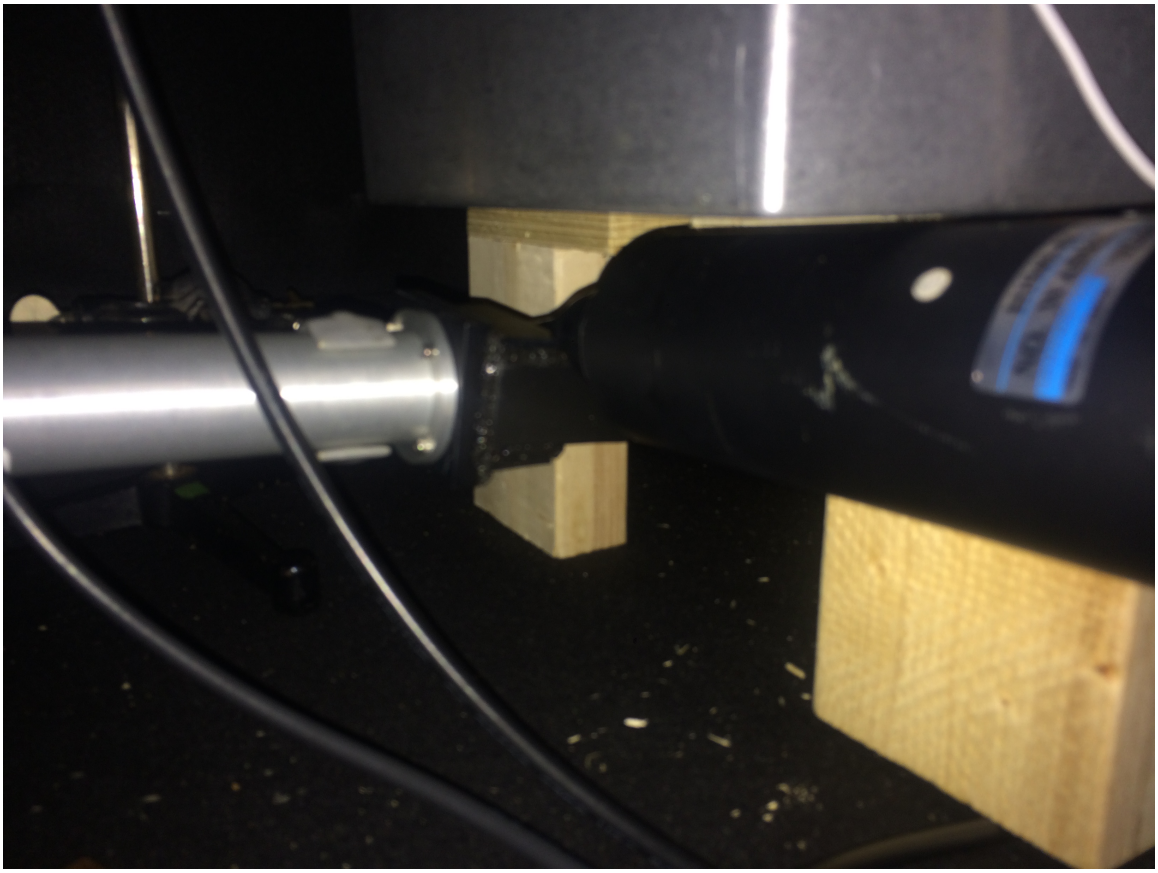

Figure 3.5: Scintillator paddle setup, which was to place two scintillator paddles below the detector. On the bottom is a thicker scintillator paddle, meant to both capture and stop most high energy events capable of causing a coincidence event, and the top one is a thin one that minimizes the amount of particles The detector is enclosed in an aluminum box above.

constructed with the goals of the experiment and with the capabilities of the detectors and peripheral attachments in mind.

The silicon strip detector was enclosed in a housing with a metal base and a plexiglass lid. Two breakout boards were used that acted as adapters for the detector channel connections that allowed the silicon detector to interface with the QWAD, one with a BNC connection for the high voltage connection on the silicon plane detector. These breakout boards attached to the detector via ribbon cables. The detector was

screwed into the base of its housing to hold it in position. Small openings shielded with thin pieces of tape were cut into the lid and the base over and under the active area of the detector, which allowed for more beta particles to pass through.

A scintillator paddle was positioned below the housing using a ring stand to facilitate a parallel placement to the housing that contained the silicon strip detector. A bench was used to elevate the detector housing over the scintillator paddle that had a channel cut through it that allows for ionizing radiation to pass through. The width of this channel in the bench is equal to the width of the scintillator paddle. A second scintillator paddle was placed above the housing, held perpendicular with a ring stand as shownin figure 3.5.

The QWAD is electrically to the silicon strip detector through the breakout boards. In all the experiments where the QWAD was used in conjunction with the silicon strip detector, the metal casing of the QWAD was not used since we either had ways to sharply filter out external noise or we were simply interested in analyzing the performance of the QWAD unshielded for various applied external threshold voltages. As with the experiments detailed in the previous section, the QWAD was powered with +5V and -5V. Threshold settings for the QWAD are described in greater detail in the following subsection. The power supply used to power the QWAD was placed next to it. Tthe only viable channel bank that could be explored was the centre channel bank, since no channels had to be run to ground. This channel bank was connected via a ribbon cable to the DAQ.

A cable was made that applied the same voltage across all 16 of the tested channels of the QWAD. By doing this, we were then allowed to adjust the voltage constantly

across all 16 channels that were being observed in a given experiment. The voltages were all applied to the corresponding header pins for each QWAD channel, as was done in the tests mentioned in the paragraph above. This provided a second way of externally adjusting the threshold across all channels to see what the response would be at each level of threshold voltage.

Everything was enclosed within a light-tight box that allowed for the ribbon cable and the power cable for the QWAD's power supply to pass through the lower part of the door. A pass-through for BNC and SHV connections on the side allowed for powering of the detectors as well as the ability to obtain the signal from the scintillator's PMT. A light-tight box is necessary whenever an experiment necessitated the usage of a PMT-scintillator paddle assembly as the trigger source.

The DAQ system has two parts: a NIM crate with a discriminator for the trigger signal from the scintillator paddle, and a VME crate that had the main boards necessary for processing the signals. The NIM crate was used to house a discriminator, which took the negatively polarized scintillator paddle signal and gave a NIM-level output gate that could be adjusted for width whenever the signal went over a certain threshold which was also adjustable. The threshold was set to reduce the number of events due to random noise while still allowing scintillator events to be detected, while the NIM gate width was within the neighbourhood of 600ns. Having the discriminator be in its own crate also allowed us to avoid any addressing conflicts that might have arisen due to read requests being made on the VME crate. After generating the NIM trigger with this discriminator, the signal was then sent on to the VME crate shown in figure 3.6.

The trigger signal is formed via passing the two scintillator paddle discriminator responses to a single AND gate. After this initial delay, the signal from the AND gate was sent to a logic gate unit that was set to OR mode to split the NIM gate into two equally timed NIM gates which were then passed on to a second logic gate board. This second board then simply acted as a NIM-level translator which gave two signals, one that had the opposing logic behaviour, and one the same logic behaviour but delayed by the same length of time as the first signal to allow both signals to have the same timing. These two signals were then sent to NIM inputs on a V1495 unit.

The V1495 is set up with the FW1495SC multievent scaler firmware that allows us to gather raw counts from the QWAD channels directly. 16 of the 64 available LVDS channels were unmasked since we were only looking at one channel bank of the QWAD at a time. The ribbon cable from the QWAD is then attached to these unmasked channels with an adapter. Counting begins upon the introduction of a NIM trigger, in our case the NIM gate described above, to the first NIM input which is used to gather triggers. Any LVDS events from that point on are counted in any of the channels that are unmasked. In order to restrict the window of counting, a second NIM signal is used that is in the opposing logic state as the NIM gate and then applied to the second NIM input which was set to an inhibit mode. This way, only events that arrive within the counting window are counted among the events. The counts are cleared with each trigger.

The frontend program was written using the basic CAENVME C libraries that are distributed with CAEN software. In the end, the only board that needed to be used

for these experiments was the V1495, so there was only one VME board that needed to be addressed. Error handlers and event screeners that filter out any unwanted messages from the V1495 were programmed in. The software worked by constantly polling the V1495 to see if it had any events. If it did, it would then take those events and write the raw text of the event to the file. Each event was set up to have the time of the trigger signal arrival as well as the counts for each channel. This would allow us to obtain rate information from the V1495, and therefore render the data from the QWAD into a useful format that could be analyzed later.

For source testing, the source used made of ^{90}Sr with a nominal activity of 1MBq. This source was chosen because it is a pure beta source, so the silicon strip detector would be responsive to it. It was housed in a plastic tube and placed on top of the detector while encased in a lead housing. Two sets of runs were taken with the source to keep track of any actual events due to the source. The other runs were taken without the source to characterize any backgrounds that would be present in our setup.

For the purpose of analysis, we treat the entire segment of the detector being studied as a single unit.

3.2.2 Timing

First, we assumed that the time it takes for ionizing radiation to travel to the scintillator paddle below the silicon strip detector is less than 10ns. In order to guarantee this assumption, the time it takes ionizing radiation to travel the space between the detectors will be computed for each case. Second, we have to take the measurement

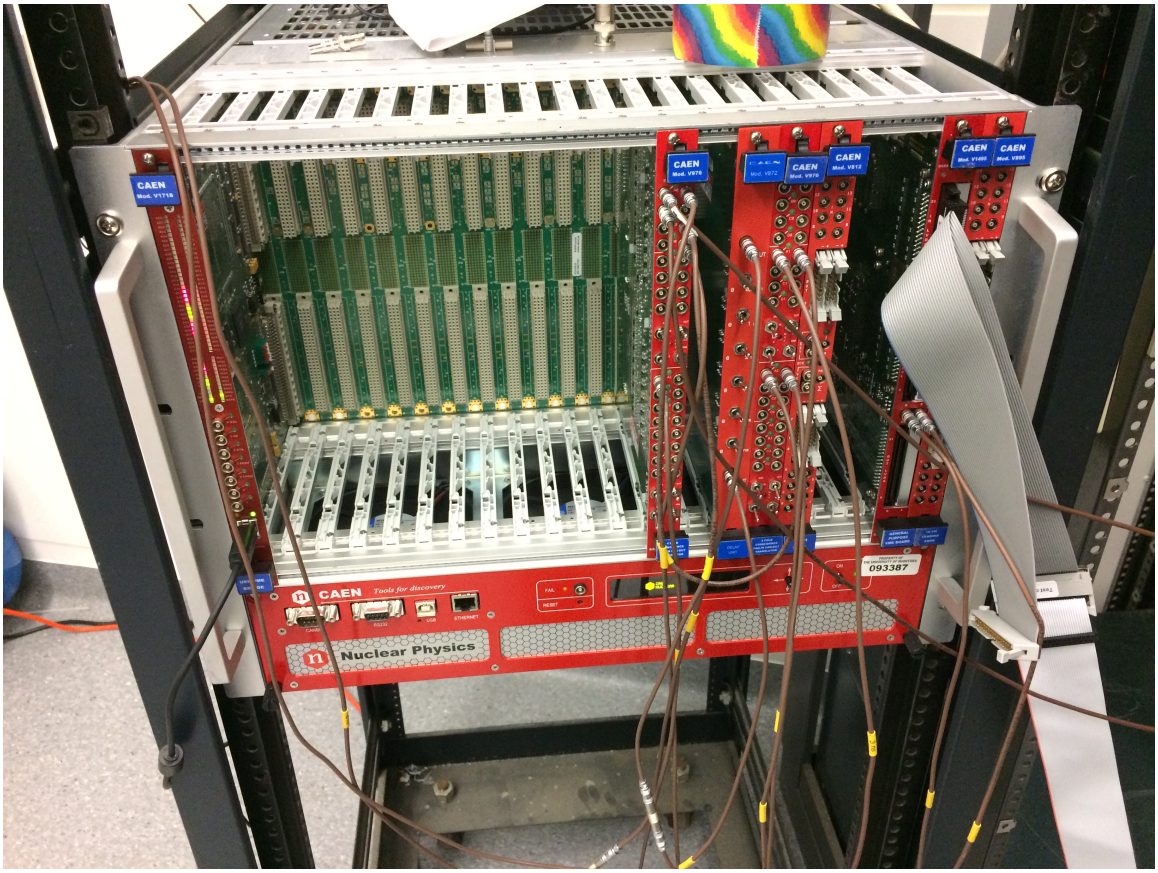

Figure 3.6: The VME crate setup used in the experiment. On the left is the board that is used to communicate with the computer that controlled the experiment. To the right of that is the coincidence gate logic units and delay units that formed the trigger. The ribbon cable is plugged into the V1495.

of the LVDS response as it enters the V1495. This is achieved by measuring the signal at the end of the ribbon cable.

It was found that the QWAD took roughly 130ns to process an event after it came from the silicon strip detector and was processed by the channel's electronics and arrived at the V1495 as shown in figure 3.7. Events that were processed are lengthened before going through the comparator as part of the time-over-threshold capabilities of the QWAD, so this results in an LVDS pulse that is significantly widened and spends

ample time in the "logic high" state. This often manifests itself as a 500ns-long LVDS pulse that starts approximately 100ns after the event from the silicon strip detector arrives. We only need to sample the beginning of this logic high state to record the event, so a trigger gate of 600ns in width arriving not soon after the event should be long enough to record that event.

With these considerations in mind, the signal from the scintillator paddles was delayed by a lenght of time around 50ns and then used as the trigger for the scaler.

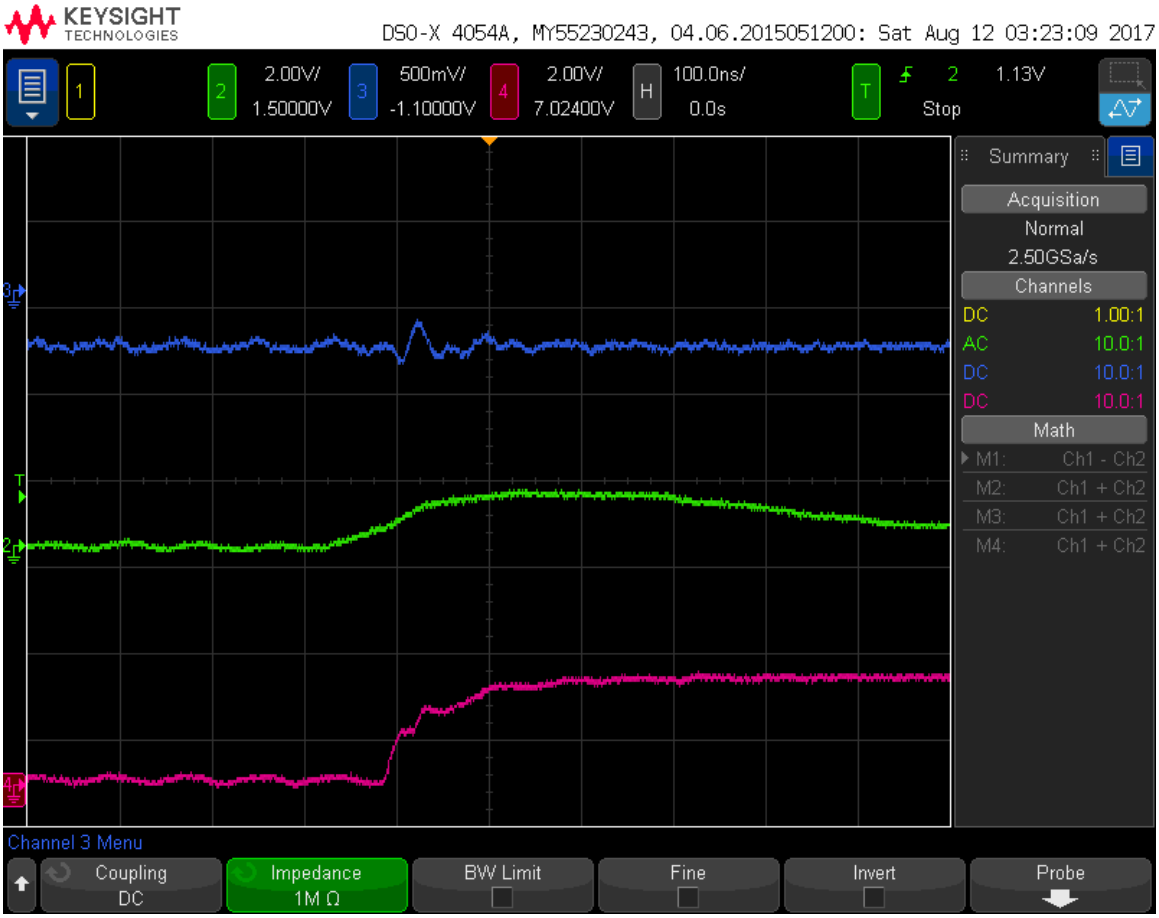

Figure 3.7: The QWAD repsonse to a beta particle event from a silicon strip detector. Channel 3 is the silicon detector response measured at the point as it enters the QWAD, channel 2 is the analog response from the QWAD amplifiers, and channel 4 is half of the LVDS response.

3.2.3 Noise

Even though the threshold modifications did allow us to eliminate the noise, there was still noise that came from a periodic "ringing" that happened every so often. This ringing was on the order of 5MHz-7MHz, and would occur spontaneously. The ringing was reduced using some magnetic cores and some additional grounding measures in an attempt to remove it. However, these preventative measures were not perfect and there would be noise that would appear in both the analog and digital signal positions of the QWAD channels as shown in figure 3.8, and this would occurr across all channels.

Within our counting window, this ringing would show up as 3 or 4 hits in that channel on the scaler. However, whenever a beta particle went through the detector the signal from that would be stronger than the noise. Because of this, we could make a cut on any scaler data to filter out noise from signal in software.

Figure 3.8: The periodic noise that was occasionally observed. The blue and the red signals are the analog and digital responses respectively. This could be reduced through the use of magnetic cores, but it would still show up every so often in spite of such fixes being implemented. This necessitates correcting for this noise in software.

Chapter 4

Results and Analysis

In this chapter I will discuss the results of the tests described in the previous chapter. It is clear from the pulse tests that the QWAD does correctly produce logic pulses in response to an analog pulse signal. Tests with the detector showed that the QWAD does amplify signals from the detector and then discriminates them properly.

4.1 Analysis of Rate Tests

The digital rate tests are counting experiments, and must be analyzed as such. In this section the rules for analyzing the data from the digital rate tests are developed.

4.1.1 Counting

The scintillator counts are straightforward in that the total number of events that are gathered over an interval of time T is directly equivalent to the count of coincidences between scintillator paddles. Since the event trigger is formed via an AND gate operation involving the signals from the two scintillator paddles, the raw count of

triggers gathered by the V1495 scaler will be equivalent to this.

Obtaining the counts for the detector is a different matter. The silicon strip detector consists of 198 individual channels, with 16 of them capable of being instrumented at any time. Since the timing window was selected so that silicon strip events would only cause one hit in that window, a cut was made on the data where only single counts would be accepted as actual data. These counts would be totalled together to obtain the total counts across all 16 instrumented channels, treating them all as one unit since there was not sufficient data to analyze the detector on a strip-by-strip basis.

Given that the expected result would be a single count within 600ns, the data was filtered for noise. If an event had multiple counts within the same window, that event was treated as noise.

4.1.2 Rates and Uncertainties

In general, a rate will have the form of:

$$R = \frac{n}{T}, \tag{4.1}$$

where n is the total number of events and T is the period of time over which these events happened. This period over which the events occurred is computed via finding the difference between the start time t_{start} and the end time t_{end} and subtracting the start time from the end time as follows:

$$T = t_{end} - t_{start}. \tag{4.2}$$

The rules for obtaining the count n were established in the previous subsection. For obtaining T, we get that from the computer using a function that gathers the

system time at the beginning and the end of each experimental run. This gives us both the pieces needed to compute the total rate in the detector and the total scintillator rate for each run.

The general form of the uncertainties from the digital rate tests (ΔR) is:

$$\Delta R = \sqrt{\left(\frac{\Delta n}{T}\right)^2 + \left(\frac{n\Delta T}{T^2}\right)^2}. \tag{4.3}$$

In order to calculate the total uncertainty we must understand first what the uncertanties in the count Δn, and the uncertainty in the period ΔT are.

For our period, we compute the uncertainty as:

$$\Delta T = 2\Delta t, \tag{4.4}$$

where Δt is the uncertainty in the individual time measurements. Time measurements taken from the computer can be thought of to have a Δt of the clock cycle of the processor since the trigger signal can arrive at any moment during a single clock cycle. This gives us a total uncertainty of the period on the order of 600ps.

For scintillator rates where we use the total number of events that are taken for a given run, the uncertainty is equivalent to the square root of the total events taken over the course of a run or $n_{scintillator}$. The other rates which depend on the number of individual counts in an individual channel of the QWAD board can be treated similarly. In the case of uncertainties of all the QWAD channel counts taken together, n_{QWAD}, we can take that total's square root to obtain it.

If we take the basic form of the rate equation and apply our considerations for each of the types of rates that are obtained from the experiments that have been performed, we get that for rates that only take into consideration the scintillator

trigger rate, or $R_{scintillator}$, the uncertainty will be:

$$\Delta R_{scintillator} = \sqrt{\left(\frac{\Delta n_{scintillator}}{t_{end} - t_{start}}\right)^2 + \left(\frac{2n_{scintillator}\Delta t}{(t_{end} - t_{start})^2}\right)^2}. \tag{4.5}$$

Similarly we obtain for the QWAD channel rates, that the uncertainties ΔR_{QWAD} will have the form:

$$\Delta R_{QWAD} = \sqrt{\left(\frac{\Delta n_{QWAD}}{t_{end} - t_{start}}\right)^2 + \left(\frac{2n_{QWAD}\Delta t}{(t_{end} - t_{start})^2}\right)^2}. \tag{4.6}$$

This suffices for obtaining the uncertainties based off error in counts and measurement alone. However, in this experiment there are various systematic uncertainties that have not been taken into account due to the spread of scintillator rates that must be compensated for in our final uncertainties. A quick way to estimate the contribution of systematic uncertainties under the experimental conditions is to find the mean and standard deviation of the two distributions of scintillator rates, both with a source and without a source, and then divide the standard deviation by the mean to obtain a constant fraction uncertainity ΔR_{syst} for each rate in that set of data as:

$$\Delta R_{syst} = \frac{\sigma_R}{\bar{R}} R. \tag{4.7}$$

Our systematic uncertainty is estimated in this way for both the source runs and the sourceless runs independently, and this is added to both detector and scintillator rate uncertainities, here represented as R_{meas}, in quadrature to obtain an R_{total} of:

$$\Delta R_{total} = \sqrt{\Delta R_{syst}^2 + \Delta R_{meas}^2}. \tag{4.8}$$

A similar uncertainty contribution due to systematic uncertainties in the detector could not be obtained due to a lack of data at each threshold level that would allow

us to similarly estimate the systematic contributions due to the detector system being tested.

4.2 Results of Rate Tests

10 runs were completed, 5 background runs where the source was not introduced and 5 runs where the source was present. Only the runs with a threshold of 2.5V were repeated. First the relevant rates are calculated, and then the relative efficiencies are found and compared to the ideal efficiency.

4.2.1 Rates

Table 4.1 gives summaries for each of the runs. Each of the background runs were taken over a duration of approximately 7 hours, and each of the source runs were taken over a duration of 3 hours. Each of these detector rates is the rate of single strip events where only one event occurred. For the threshold voltages, four voltages from 2.5V to 2.8V were used the values used to compute all these were taken from Appendix B.

4.2.2 Relative Efficiencies

To obtain the relative efficiency ϵ_{rel} for a given threshold level, we calculate it using:

$$\epsilon_{rel} = \frac{R_{det}/R_{scint}}{R'_{det}/R'_{scint}}. \tag{4.9}$$

Where the rates R'_{det} and R'_{scint} are the rates of the detector and the scintillator paddle taken at the lowest threshold voltage that was applied to the QWAD. The

Background Runs				
Threshold	R_{scint} **(Hz)**	ΔR_{scint} **(Hz)**	R_{det} **(Hz)**	ΔR_{det} **(Hz)**
2.8V	0.114	0.005	0.0005	0.0002
2.7V	0.109	0.005	0.0011	0.0002
2.6V	0.104	0.005	0.0012	0.0002
2.5V	0.113	0.005	0.0019	0.0003
Source Runs				
Threshold	R_{scint} **(Hz)**	ΔR_{scint} **(Hz)**	R_{det} **(Hz)**	ΔR_{det} **(Hz)**
2.8V	1.3	0.1	0.14	0.01
2.7V	1.5	0.1	0.19	0.02
2.6V	1.5	0.1	0.102	0.008
2.5V	1.3	0.1	0.15	0.01

Table 4.1: Collected rates for all runs

uncertainties for each relative efficiency are found using:

$$\Delta\epsilon_{rel} = \left(\left(\frac{R'_{scint}\Delta R_{det}}{R'_{det}R_{scint}} \right)^2 + \left(\frac{R_{det}\Delta R'_{scint}}{R'_{det}R_{scint}} \right)^2 + \left(\frac{R_{det}R'_{scint}\Delta R_{scint}}{R^2_{scint}R'_{det}} \right)^2 + \left(\frac{R_{det}R'_{scint}\Delta R'_{det}}{R'^2_{det}R_{scint}} \right)^2 \right)^{\frac{1}{2}}. \quad (4.10)$$

For the final relative efficiencies, we were obtained the following values in the table 4.2, and then the relative efficiencies are plotted for the sources in figure 4.1.

Background Runs		
Threshold	ϵ_{rel}	$\Delta\epsilon_{rel}$
2.8V	0.29	0.09
2.7V	0.6	0.2
2.6V	0.7	0.2
2.5V	1.0	0.2
Source Runs		
Threshold	ϵ_{rel}	$\Delta\epsilon_{rel}$
2.8V	0.9	0.1
2.7V	1.2	0.2
2.6V	0.58	0.09
2.5V	1.0	0.2

Table 4.2: Relative efficiencies for our selected runs.

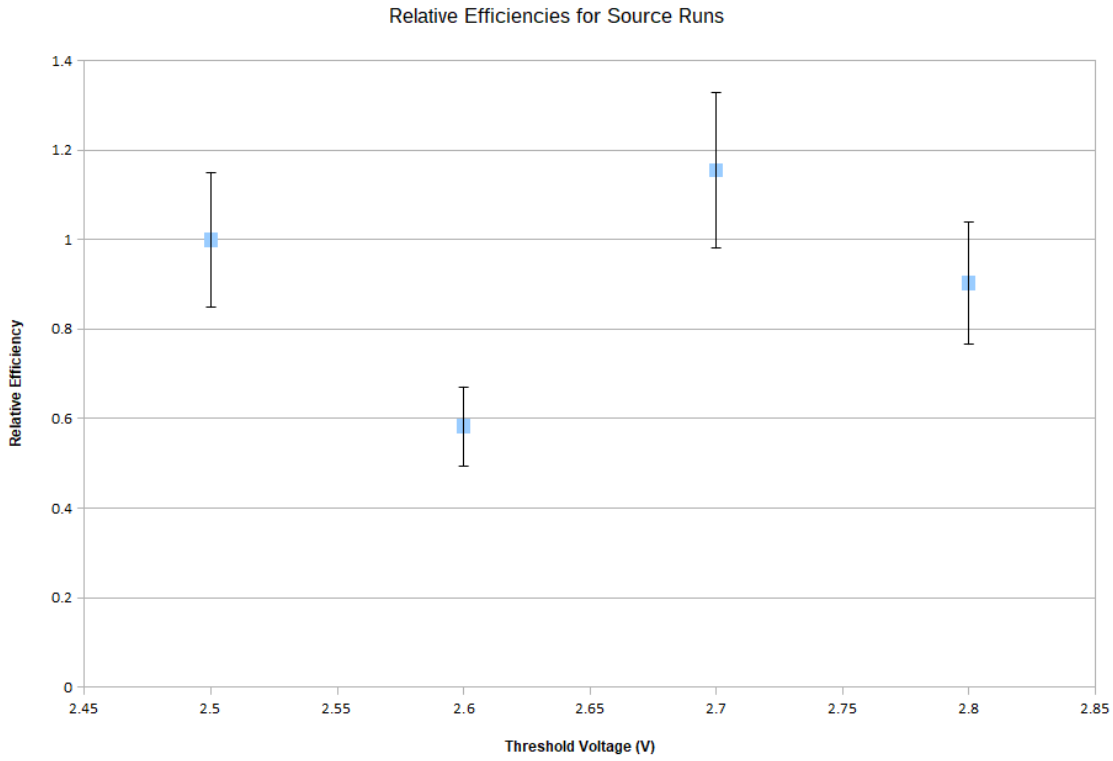

Figure 4.1: Here are the relative efficiencies plotted as a funciton of voltage for the data runs that used a source. As threshold voltage increases, more signal should be cut off which should result in a downward trend in relative efficiencies. This was not observed due to various systematic factors that were not previously accounted for.

Chapter 5

Conclusion

Increasing the precision of polarimetry measurements is important for experiments that use parity-violating electron scattering. To this end, it is necessary to measure the scattering asymmetry of Compton-scattered electrons as a function of distance from the beamline. The Hall A Compton polarimeter has gone through upgrades to work with the higher energy beam that can now be produced at JLab. However, the electron detector that is presently used in Hall A exhibits an unacceptable noise response that impedes precise polarimetry meaurements in the lab environment. The Hall A electronics do not employ a time-over-threshold capability to give us a further criteria for filtering signal from noise, but the QWAD does.

In the previous chapters it was established that there is a need for precise polarimetry at JLab for the purpose of experiments involving parity-violating electron scattering. Compton polarimetry will allow for the measurement of the polarization of the beam to occur simultaneously with other experiments. It was hypothesized that the QWAD working in conjunction with a plane from the silicon strip detector

would provide a solution to eliminating noise from data in the Hall A polarimeter.

From the tests with the QWAD alone it can be seen that the QWAD does function as intended. It responds to pulse signals from function generators with digital signals. However, there was a fair bit of noise, and further modifications to the potentiometers to increase the range of internal threshold voltages are necessary to filter noise when used in conjunction with the silicon strip detector. However, until such a change can be implemented, all future tests of the QWAD will require an additional external voltage to be applied directly to the board. Application of an external voltage across all channels with the same DC power supply will not allow for the level of control necessary when used in an experimental hall, so this modification to the potentiometers will be necessary for implementation in Hall A.

The analog and digital responses after adjusting the thresholds show that, in principle, the QWAD should work with the silicon strip detector. It responds well to the signals from the silicon strip detector in the presence of a source in scope traces as shown in Appendix A.

However, the digital rate tests ultimately show some potential flaws in the QWAD and data acquisition setup. The relative efficiencies with the sources in particular show that the efficiency does not consistently decrease with threshold voltage as would be expected, and the uncertainties that were computed with the data also shows that the detector performed poorly in the presence of a radioactive source.

There is a downward trend with relative efficiencies as a function of increased threshold voltage with respect to the background runs that were taken, which is what is expected as the threshold voltage increases. However, this same trend did not

appear in the source tests, showing there are systematic issues with the rate tests that have not been accounted for. These will have to be identified and resolved in future rate tests.

The QWAD also offers other functionalities in the amplifier-discriminator process that would enable us to further filter out noise by allowing us to look at the time over which the signal persists over the threshold. This would be an important next step in evaluating the QWAD's overall utility in Hall A.

I conclude that the QWAD is functional with the silicon strip detector in principle. Monitoring the QWAD response on an oscilloscope shows that when the silicon strip detector is connected it does discriminate events from noise with the proper adjustments to the internal threshold voltages.This shows that there is a potential future application of this board in Hall A. However, there are several systematic errors that need to be resolved in rate tests in order to assess what further modifications will be necessary to employ it in Hall A.

Appendix A

QWAD Details

In order to properly test the QWAD, the response had to be observed. Here I detail how the QWAD responds to test pulses and silicon strip detector events, as well as how to properly time a DAQ trigger for QWAD testing.

A.1 Test Pulse Responses

The QWAD responds to test pulses typically by giving an LVDS signal response that lasts 500ns after the tail end of the test pulse as shown in figure A.1. This was determined by using a signal generator and then examining the LVDS responses using a cable monitor that plugged into the second channel bank. Each QWAD response comes in two stages: first the stage from the amplifier, then the stage from the comparator. These stages are demonstrated in figure A.2.

Figure A.1: This is an example LVDS response from the QWAD. Here the first and second channels are the LVDS signals, the fourth chanel is the pulse signal, and the third channel is the trigger signal. Here the remainign waveform indicates the voltage taken when the two signals are subtracted from each other, demonstrating how LVDS logic states are processed.

A.2 Silicon Detector Response

The QWAD had a different response for test pulses than it does for silicon detector signals as shown in figure A.3. The LVDS signal length tracked the length of time that it spent over the threshold that was set.

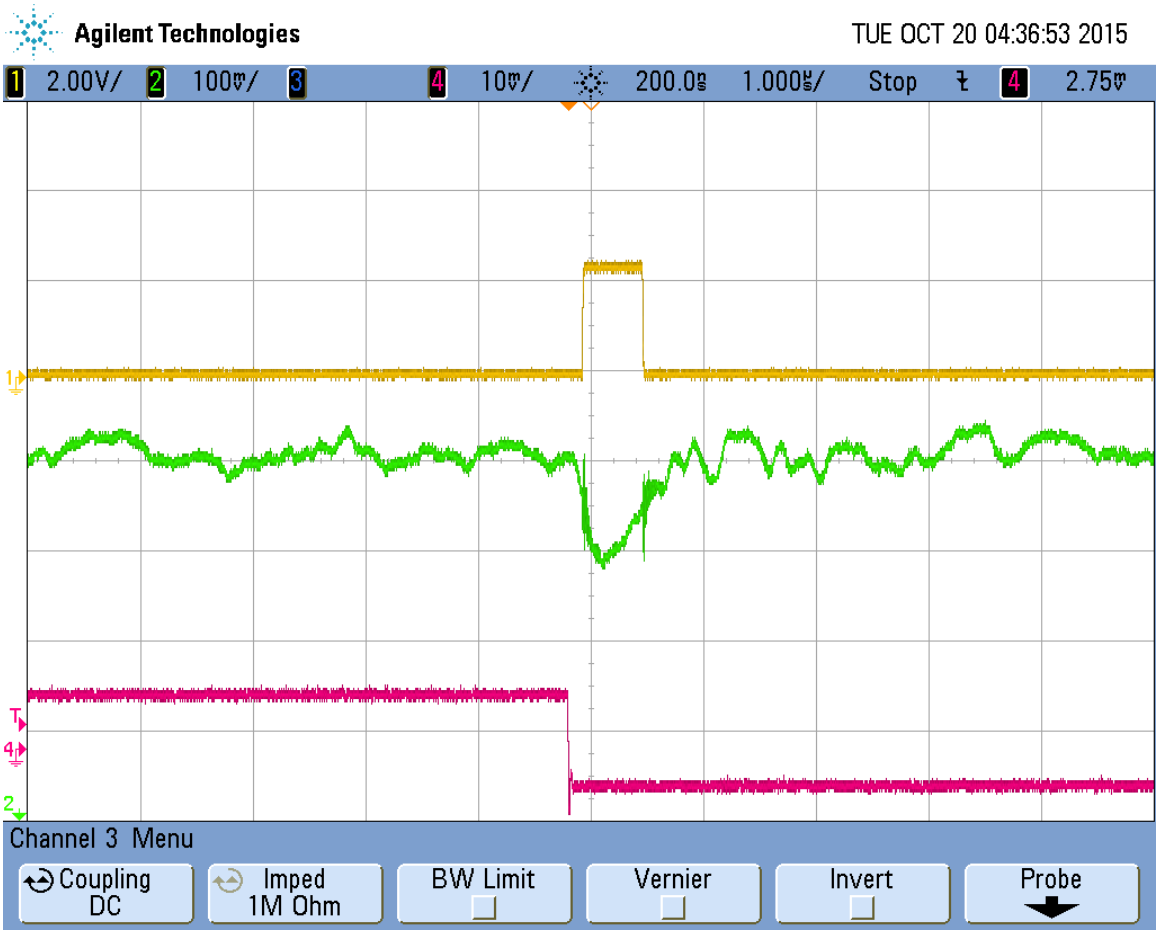

Figure A.2: The analog response of the QWAD to a test signal. Channel 4 is the test signal, channel 2 is the analog response, and channel 1 is half of the LVDS response.

A.3 DAQ Timing

The problem of determining the timing for the DAQ system so that the QWAD signals and the scintillator signal trigger arrive at the same time is resolved by finding out how long it takes the QWAD to respond to a silicon strip detector event and then determine the best timing from there. Using this method, and it was found that the signal response went to "logic high" after approximately 130ns as shown in figure 3.7.

Upon establishing this timing window, we tested the overall timing with a signal

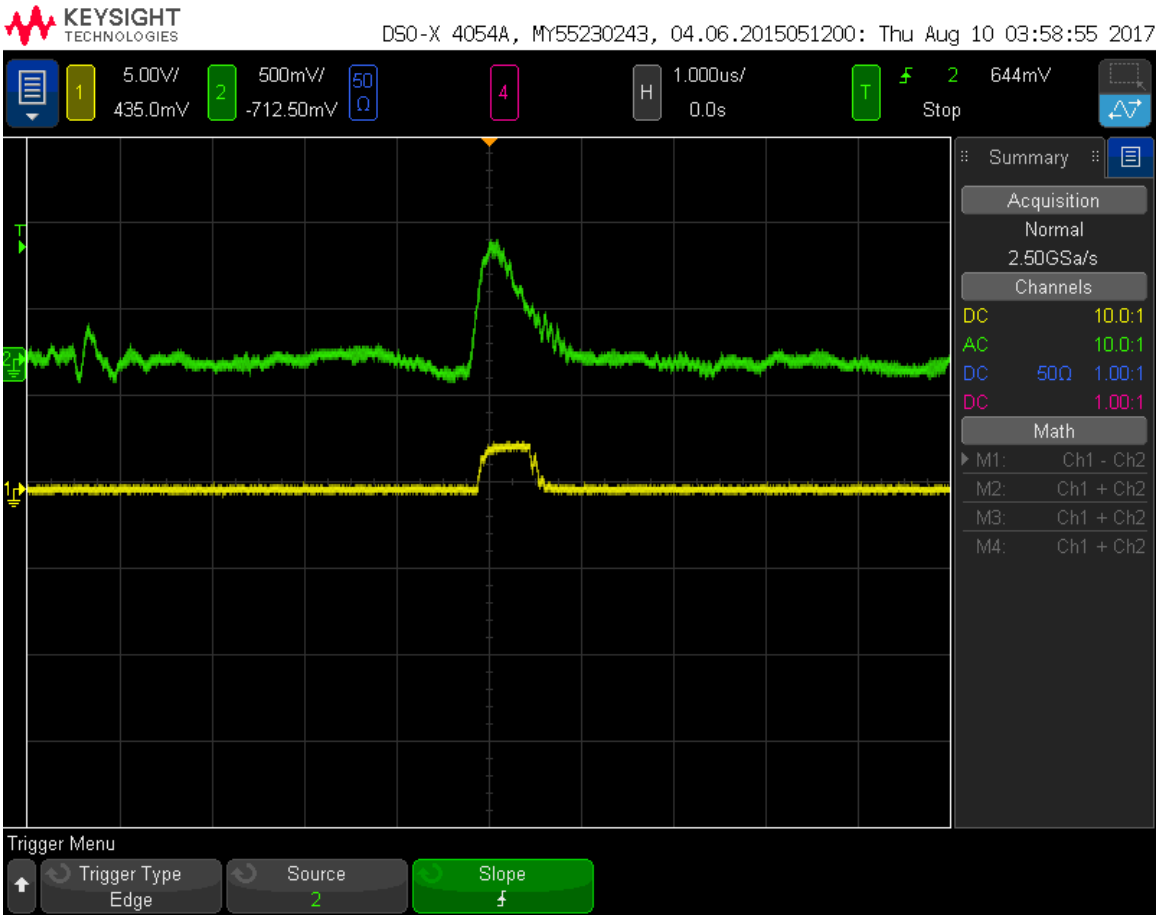

Figure A.3: The response to a beta particle causing an event in the silicon strip detector. Channel 2 is the analog response and channel 1 is half of the LVDS signal.

generator. The sync signal, or the signal from the pulse generator that was used for stood in for the scintillator paddle signal, and a test pulse was used at the same time with the QWAD to confirm the delays all matched as shown in figure A.4.

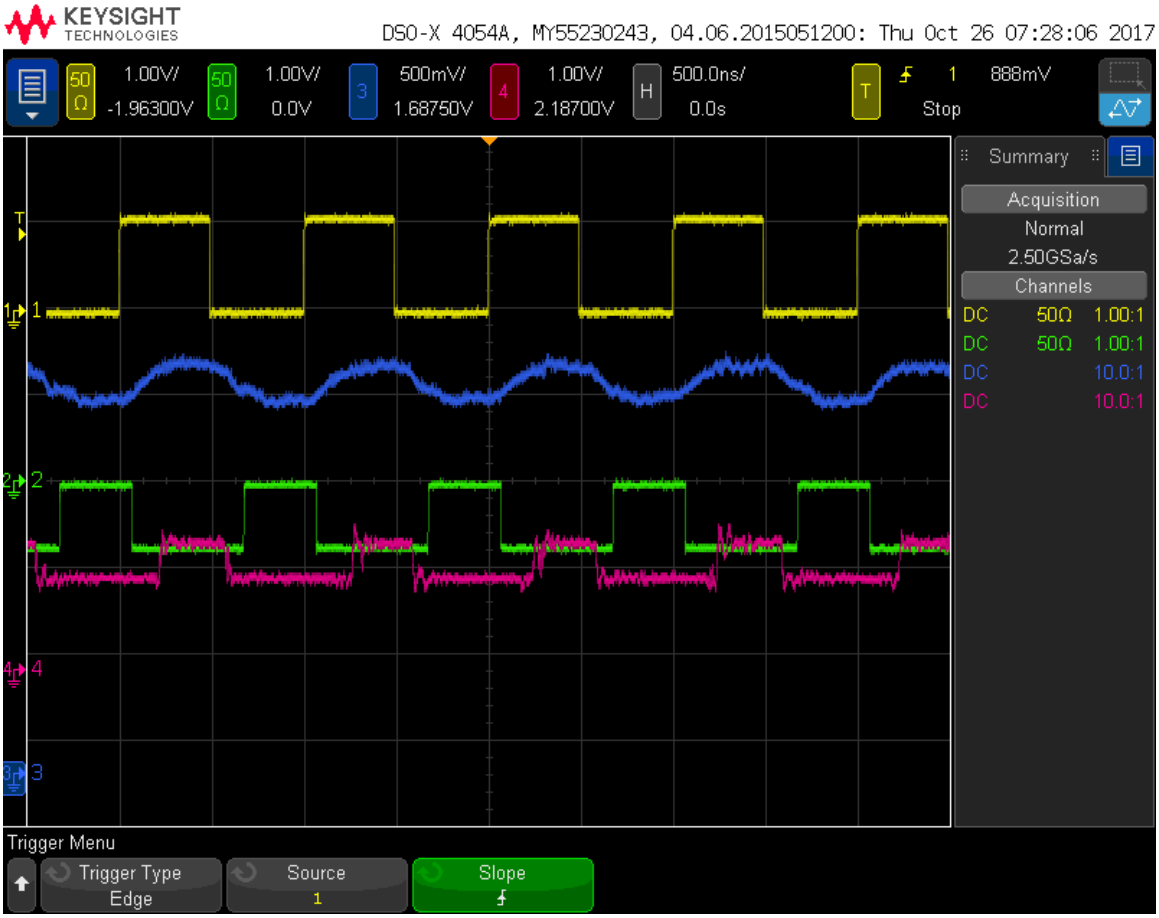

Figure A.4: This scope trace demonstrates the timing of the trigger signal in the DAQ system. Channel 2 is the trigger gate signal, channel 1 is the synch signal used to obtain this gate and the third and fourth channels are the analog signal and the digital signal from the QWAD respectively. This shows that the scintillator paddle trigger will come in time with the QWAD events.

Appendix B

Full Results for Digital Rates Tests

The tables B.1,B.2, B.3, and B.4 in this chapter show the full results of each of the runs taken for this experiment. The runs are grouped by thier respective threshold voltages. The run duration in seconds, the number of scintillator events, and the number of total hits in each channel are presented in the first couple of tables. The last two tables have the number of single hits in each of the channels sorted by threshold voltage for the respective run. These tables are further distinguished by having the data for background runs and having the data for source runs.

Threshold (V)		2.5	2.6	2.7	2.8
Time (s)		10800.70	10800.70	10800.39	10800.35
Scintillator Counts		14263	16483	15815	14302
Channel Counts (Total Hits)	**1**	39843	473	709	44081
	2	195048	729	1133	220173
	3	39017	241	404	43930
	4	39014	142	421	43926
	5	38038	167	378	43966
	6	38981	398	758	43905
	7	39038	181	374	43949
	8	38874	245	264	43829
	9	39011	470	298	43920
	10	39016	161	412	43927
	11	39014	180	430	43939
	12	38965	211	458	43898
	13	38971	0	0	0
	14	6	0	17	33364
	15	38982	688	432	43951
	16	39038	156	429	43974

Table B.1: Total hits in channels for source tests.

Threshold (V)		2.5	2.6	2.7	2.8
Time (s)		25203.39	25219.74	25201.61	25205.57
Scintillator Counts		2841	2621	2745	2866
Channel Counts (Total Hits)	**1**	8003	5728	6484	1050
	2	39483	13294	38644	4096
	3	7972	2659	6413	824
	4	7911	2654	6401	824
	5	8020	2659	6405	824
	6	8031	2662	6395	821
	7	7929	2662	6401	822
	8	7844	2653	6381	823
	9	7936	2661	6393	823
	10	7975	2657	6404	822
	11	8044	2655	6397	826
	12	7955	2664	6392	827
	13	7975	0	0	0
	14	7998	2055	6370	825
	15	8020	2660	6400	825
	16	8001	2667	6405	827

Table B.2: Total hits in channels for background tests.

Threshold (V)		2.5	2.6	2.7	2.8
Channel Counts (Single Hits)	**1**	118	66	195	102
	2	13	91	186	22
	3	113	44	162	105
	4	115	47	205	105
	5	113	43	171	106
	6	114	59	129	107
	7	115	36	178	106
	8	118	96	95	106
	9	118	354	106	105
	10	114	27	161	106
	11	117	50	173	109
	12	114	39	123	105
	13	115	0	0	0
	14	6	0	2	81
	15	115	117	90	106
	16	116	32	116	108

Table B.3: Single hits in channels for source tests.

Threshold (V)		2.5	2.6	2.7	2.8
Channel Counts (Single Hits)	**1**	2	6	1	2
	2	4	4	0	2
	3	1	0	2	1
	4	2	0	2	1
	5	2	1	2	2
	6	2	2	2	0
	7	3	1	2	1
	8	0	3	2	0
	9	14	3	2	1
	10	2	0	2	0
	11	3	0	2	1
	12	2	1	2	0
	13	3	0	0	0
	14	3	6	3	1
	15	1	2	2	1
	16	4	1	2	1

Table B.4: Single hits in channels for background tests.

Bibliography

[1] A.H. Compton, *A Quantum Theory of the Scattering of X-Rays by Light Elements*, Phys. Rev. **21** (1923) 715.

[2] M. Hauger et al., "A high-precision polarimeter", Nucl. Instrum. Methods Phys. Res. A **462** (2001) 382.

[3] W. R. Leo, *Techniques for Nuclear and Particle Physics Experiments*, 2nd edition, Springer-Verlag, 1994

[4] David J. Griffiths, *Introduction to Electrodynamics*, 3rd edition, Prentice Hall, 1999

[5] John David Jackson, *Classical Electrodynamics*, 3rd edition, John Wiley & Sons Inc, 1999

[6] K. Paschke et. al, "PREX-II: Precision Parity-Violating Measurement of the Neutron Skin of Lead"

[7] J. Mammei et. al, "CREX: Parity-Violating Measurement of the Weak Charge Distribution of ^{48}Ca to 0.02 fm Accuracy"

[8] G. Bardin et. al, "Conceptual Design Report of a Compton Polarimeter for Cebaf Hall A", May 9, 1996 (unpublished)

[9] Amrendra Narayan, PhD, Mississippi State University, 2015

[10] Stéphanie Escoffier, PhD, Université Paris 7, 2001

[11] Michael H. McDonald, Honours BSci, University of Winnipeg, 2008

[12] MJ Muslof et. al, "Intermediate-Energy Semileptonic Probes of the Hadronic Neutral Current", Physics Reports 239, Nos. 1 & 2, 1-178, 1994

[13] Ya. B. Zel'dovich, "Parity Nonconservation in the First Order in the Weak-Interaction Constant in Electron Scattering and Other Effects", J. Exptl. Theoret. Phys. (U.S.S.R.) 36, 964-966, March, 1959

[14] B. Joly, M. Magne, M. Brossard, M. Crouau, R. Bonnefoy, C. Camacho, "Tests of an electron detector system with cosmic muons for JLab Hall A Compton polarimeter", May 15, 2012

[15] J.M. Grames et al, "Unique electron polarimeter analyzing power comparison and precision spin-based energy measurement"', Physical Review Special Topics - Accelerators and Beams, Volume 7, 042802, 2004

[16] Technical Information Manual for MOD. FW1495SC, Revision n. 6, CAEN SpA, 2016